

Received XX Month, XXXX; revised XX Month, XXXX; accepted XX Month, XXXX; Date of publication XX Month, XXXX; date of current version January, 2026.

Digital Object Identifier 10.1109/OJCOMS.xx.xx

AFDM: Evolving OFDM Towards 6G+

Hyeon Seok Rou¹ (Member, IEEE),
Vincent Savaux² (Senior Member, IEEE), Zeping Sui³ (Member, IEEE),
Giuseppe Thadeu Freitas de Abreu¹ (Senior Member, IEEE),
and Zilong Liu³ (Senior Member, IEEE)

¹School of Computer Science and Engineering, Constructor University Bremen, Campus Ring 1, 28759 Bremen, Germany

²Institute of Research and Technology b-com, 35510 Cesson Sévigné, France

³School of Computer Science and Electronics Engineering, University of Essex, Colchester CO4 3SQ, U.K.

CORRESPONDING AUTHOR: Hyeon Seok Rou (e-mail: hrou@constructor.university).

ABSTRACT As the standardization of sixth generation (6G) wireless systems accelerates, there is a growing consensus in favor of *evolutionary* waveforms that offer new features while maximizing compatibility with orthogonal frequency division multiplexing (OFDM), which underpins the 4G and 5G systems. This article presents affine frequency division multiplexing (AFDM) as a premier candidate for 6G, offering intrinsic robustness for both high-mobility communications and integrated sensing and communication (ISAC) in doubly dispersive channels, while maintaining a high degree of synergy with the legacy OFDM. To this end, we provide a comprehensive analysis of AFDM, starting with a generalized fractional-delay-fractional-Doppler (FDFD) channel model that accounts for practical pulse shaping filters and inter-sample coupling. We then detail the AFDM transceiver architecture, demonstrating that it reuses nearly the entire OFDM pipeline and requires only lightweight digital pre- and post-processing. We also analyze the impact of hardware impairments, such as phase noise and carrier frequency offset, and explore advanced functionalities enabled by the chirp-parameter domain, including index modulation and physical-layer security. By evaluating the reusability across the radio-frequency, physical, and higher layers, the article demonstrates that AFDM provides a low-risk, feature-rich, and efficient path toward achieving high-fidelity communications in the later versions of 6G and beyond (6G+).

INDEX TERMS Affine frequency division multiplexing (AFDM), orthogonal frequency division multiplexing (OFDM), evolutionary, 6G and beyond (6G+), backward compatibility, system reusability.

I. Introduction

A. Background

It is widely anticipated that sixth generation (6G) systems will usher in transformative advances across both technological and application domains, far surpassing the incremental gains realized in the transition from fourth generation (4G) to fifth generation (5G) systems [1]–[3]. Besides the development of new 6G use cases, such as the integration of artificial intelligence (AI) technology and integrated sensing and communication (ISAC) functionalities, this evolution will also be shaped by crucial decisions [4]–[6] recently reached by 3GPP, reaffirming the use of orthogonal frequency division multiplexing (OFDM), specifically cyclic prefix orthogonal frequency division multiplexing (CP-OFDM) and discrete Fourier transform spread orthogonal frequency division multiplexing (DFT-s-OFDM), as the baseline waveform for

6G [7]–[10]. This choice was motivated by the maturity of OFDM technology, which has been tried-and-tested through wide deployment in multiple wireless systems that culminate in a vast experience in practical implementation. A wide range of techniques such as peak-to-average power ratio (PAPR) reduction [11], carrier frequency offset (CFO) calibration [12], and advanced channel estimation and tracking methods [13], [14], have been developed and proven effective in mitigating inherent limitations of OFDM, further strengthening it as a solid foundation for the sixth generation (6G) air interface design [15].

However, the aforementioned decision should not be perceived that the 6G waveform is finalized. In fact, 3GPP leaves the door open for investigating new waveforms designed to address the limitations of OFDM in future 6G use cases and to facilitate the integration of multiple functionalities, such as sensing and computing.

The message is that the candidate waveform solutions for later versions of 6G and beyond (6G+) must remain closely aligned with the OFDM legacy, emphasizing backward compatibility, coexistence, and hardware reusability [4]. This creates a stringent requirement: any waveform proposed for 6G+ must reuse, to the greatest extent, the existing OFDM infrastructure, while simultaneously addressing challenges that conventional OFDM cannot overcome. Firstly, the next-generation waveforms must be able to deal with a series of deteriorating effects incurred by the high mobility channels [16] and/or high frequency bands (e.g., millimeter wave or Terahertz bands), which generally suffer from large path loss and strong phase noise and/or carrier frequency offsets. Secondly, next-generation waveforms are expected to offer improved sensing capabilities compared to OFDM counterparts [17].

These scenarios are at the core of the transformative shift envisioned for 6G+. For example, non-terrestrial networks (NTN) scenarios, consisting of satellite systems, high-altitude platform station (HAPS), and flying drones [18], [19], are characterized by the inherently high moving speeds that will inevitably induce Doppler shifts/spread far beyond the tolerance of OFDM, even under advanced mitigation strategies.

Similarly, in direct device-to-device (D2D) and sidelink communications, which are expected to play a central role in 6G for applications such as vehicle-to-vehicle (V2V) and vehicle-to-everything (V2X), or drone-to-drone connectivity [20]–[22], the non-stationary mobile channels and the lack of centralized synchronization further expose the vulnerability of OFDM to Doppler impairments [23].

An additional dimension arises with ISAC, whose demand is widely present in the aforementioned scenarios [24]–[26]. In ISAC systems, the waveform must not only support reliable data transmission but also enable accurate estimation of the range and velocity for effective environment sensing [27], [28]. In a highly dynamic 6G system, such a requirement may not be fulfilled by OFDM as it lacks the intrinsic robustness to joint delay-Doppler variations.

B. Why AFDM?

In the context of the above, it is clear that a new waveform paradigm is needed to truly enable 6G to its full extent, one that simultaneously preserves OFDM's implementation and efficiency advantages while embracing, rather than counteracting, the characteristics of doubly dispersive channels.

To this end, affine frequency division multiplexing (AFDM) [29] has emerged recently as one of the most promising waveform paradigms. Unlike conventional OFDM, which separately modulates different information symbols onto multiple orthogonal subcarriers, AFDM employs chirp-based subcarriers whose instantaneous frequencies increase linearly over time. With the aid of the affine Fourier transform (AFT), AFDM spreads each symbol across the time and frequency domains, thereby enjoying

the full channel diversity as well as strong resilience to Doppler (an intrinsic property owned by the chirp signals).

In addition, the chirp parameters of AFDM are tunable, enabling flexible adaptation to the characteristics of the doubly dispersive channel to ensure maximum diversity for optimal communications performance over a variety of channel settings [30]–[32], in addition to the ability to support advanced functionalities such as index modulation [33]–[35] and physical-layer security [36]–[38]. In light of these advantages of the affine frequency domain, AFDM has also motivated in various derivative and related schemes exploiting the chirp-based waveform structure [39]–[45].

Furthermore, from a hardware implementation perspective, AFDM can be regarded as a direct extension and generalization of OFDM, where the latter is reduced to AFDM under specific parameter settings [30]. Namely, the transceiver processing chain of AFDM remains largely intact, with only an additional linear-complexity pre- and post-processing step applied around the conventional inverse fast Fourier transform (IFFT)/fast Fourier transform (FFT) operations of OFDM. Consequently, AFDM is inherently compatible to OFDM, allowing the reuse of key signal processing blocks such as IFFT/FFT modules, parallel-to-serial conversion, time-frequency resource management, and prefix handling. Moreover, the extensive body of OFDM enhancements, including PAPR reduction, pulse shaping, and spectral containment methods, can be applied to AFDM with only minor adaptation, given the fundamental similarity in signal structure across time-frequency subcarriers.

On the other hand, competing waveform proposals such as orthogonal time-frequency space (OTFS) [46], orthogonal time-sequency multiplexing (OTSM) [47], [48] orthogonal delay-Doppler multiplexing (ODDM) [49], and Zak-OTFS [50] adopt a fundamentally different signaling framework. Instead of operating in the time-frequency domain, as that in OFDM and AFDM, these schemes modulate the information symbols onto the two-dimensional delay-Doppler domain [51], with the aim to exploit the inherent delay-Doppler sparsity of doubly dispersive channels [16]. As a result, they have been shown to also achieve strong theoretical performance in high-mobility scenarios [52], [53].

However, such performance comes at the cost of requiring a fundamentally new system design, including different resource allocation approaches, new pilot structures and prefixing dimensions, as well as more complex multiple access schemes, none of which are directly compatible with the established OFDM framework. Consequently, their integration into existing OFDM-dominated architectures would demand extensive modifications at both the physical and higher layers, complicating backward compatibility and coexistence [30]. This requirement runs counter to recent standardization decisions favoring OFDM-based evolution and would therefore impede the prospects of such schemes being adopted without a fundamental paradigm shift.

C. Contributions of this article

A major objective of this article is to demonstrate that AFDM is a formidable candidate for next-generation air interfaces, capable of addressing the multifaceted requirements of 6G – including extreme mobility, NTN operation, D2D communications, ISAC, and PHY-security – while preserving architectural compatibility with the OFDM legacy.

Going beyond the current state-of-the-art of AFDM, highlighting its superior performance over OFDM in challenging 6G channel conditions and various use cases [28], [29], [54]–[66], this article provides a comprehensive analysis of AFDM from a practical implementation perspective. Specifically, we examine its feasibility in direct comparison with OFDM across several critical dimensions:

- Compatibility of AFDM with OFDM hardware and signal processing blocks, such as the reuse of the existing modules in OFDM systems, such as FFT, pulse shaping, and prefixing and resource management.
- Implementation complexity and overhead of AFDM compared to OFDM, in aspects such as transceiver processing, channel estimation, and detection.
- Robustness of AFDM in the presence of the challenging fractional-delay-fractional-Doppler (FDFD) conditions, channel estimation errors, and hardware impairments.
- Advanced functionalities enabled by AFDM, such as multiple access and coexistence with OFDM, chirp-domain modulation, and physical-layer security.

To wrap up, we also qualitatively evaluate the reusability of AFDM across the radio frequency (RF), physical layer (PHY), and higher layers, against the legacy OFDM systems, providing a holistic view of its potential for seamless and evolutionary integration into the 6G+ ecosystem.

D. Organization of this article

The remainder of this article is structured as follows: Section II introduces the system and channel models adopted throughout the article, including the novel formulation of a general FDFD channel input-output model based on physical pulse footprints to capture inter-sample coupling effects in practical transceiver implementations accurately; Section III details the transceiver architecture of AFDM, highlighting its compatibility and reusability with respect to OFDM, considering various aspects, such as prefixing, pulse shaping, and resource management; Section IV presents a variety of thorough analyses of AFDM in comparison with OFDM, including implementation complexity and scalability, channel estimation and detection architecture, robustness to impairments like phase noise (PHN) and CFO, and advanced functionalities including multiple-input multiple-output (MIMO), chirp-domain modulation and physical-layer security; Finally, Section V qualitatively summarizes the reusability of the presented AFDM considerations and discussion across the RF, PHY, and higher layers, followed by concluding remarks in Section VI.

Notation: Scalars, vectors, and matrices are denoted by lowercase, bold lowercase, and bold uppercase letters, respectively, e.g., x , \mathbf{x} , and \mathbf{X} . The i -th element of a vector \mathbf{x} is denoted by x_i , and the (i, j) -th element of a matrix \mathbf{X} by $x_{i,j}$. When subscripts become overly dense, the alternative notations $[\mathbf{x}]_i$ and $[\mathbf{X}]_{i,j}$ may be used for clarity. The transpose, Hermitian (conjugate) transpose, and inverse of a matrix \mathbf{X} are denoted by \mathbf{X}^T , \mathbf{X}^H , and \mathbf{X}^{-1} , respectively. The operators \otimes and \odot respectively denote the Kronecker and Hadamard product, and $*$ the linear convolution. The sets of natural, rational, integer, real, and complex numbers are denoted by \mathbb{Z} , \mathbb{Q} , \mathbb{R} , and \mathbb{C} , respectively. $\delta(\cdot)$ represents the Dirac delta function, while $\delta[\cdot]$ denotes the Kronecker delta. The modulo- N operation is represented by the operator $(\cdot)_N$.

II. System Model

We first present the continuous-time single-input single-output (SISO) doubly dispersive channel model and its corresponding discrete-time equivalent representation, leading to the general fractional-delay-fractional-Doppler (FDFD) input-output relation in matrix form, which will be used throughout this article.

A. Continuous-Time SISO Doubly Dispersive Channel

Consider a wireless channel with P significant (resolvable) scattering propagation paths, characterized by its continuous-time time-varying impulse response function (TVIRF) given by [16]

$$h(t, \tau) = \sum_{p=1}^P h_p e^{j2\pi\nu_p t} \delta(\tau - \tau_p), \quad (1)$$

where $h_p \in \mathbb{C}$ denotes the complex gain, $\tau_p \in \mathbb{R}$ denotes the propagation delay, and $\nu_p \in \mathbb{R}$ denotes the associated Doppler frequency shift of the p -th path, and the combined influence of the path delays τ_p (frequency selectivity) and Doppler shifts ν_p (time selectivity) gives rise to the so-called doubly dispersive fading environment.

The maximum delay spread and maximum Doppler spread of the channel are defined as $\tau_{\max} \in \mathbb{R}^+$ and $\nu_{\max} \in \mathbb{R}^+$, respectively, such that $\tau_p \in [0, \tau_{\max}]$ and $\nu_p \in [-\nu_{\max}, \nu_{\max}]$ for $p \in \{1, \dots, P\}$, and the channel is considered underspread if $\tau_{\max}\nu_{\max} \ll 1$, and overspread otherwise.

Then, given an arbitrary time-domain transmit signal $s(t)$, the corresponding input-output relation in the continuous-time domain is given by a linear convolution with the TVIRF in (1), which is expressed as

$$r(t) = s(t) * h(t, \tau) + w(t) = \int_{-\infty}^{+\infty} h(t, \tau) s(t - \tau) d\tau + w(t), \quad (2)$$

where $r(t)$ and $w(t)$ represent the time-domain received signal over the doubly dispersive channel and the additive white Gaussian noise (AWGN) signal, respectively.

B. Discrete-Time Equivalent Model

To represent the continuous system model in a manner compatible with discrete signal processing, the continuous-time signal is sampled at a sampling interval of $T_s \triangleq \frac{1}{f_s}$, where f_s is the sampling frequency in Hz.

Then, denoting $n \in \{0, \dots, N-1\}$ as the sample index of the discrete sequence, the discrete-time channel input-output relation is expressed as

$$r[n] = \sum_{p=1}^P h_p e^{j2\pi\nu_p n T_s} s[n - \frac{\tau_p}{T_s}] + w[n], \quad (3)$$

where $r[n]$, $s[n]$, and $w[n]$ are the sampled received, transmitted, and noise signal sequences, respectively.

Then, defining the normalized delay indices and the normalized digital Doppler shift indices as

$$\ell_p \triangleq \frac{\tau_p}{T_s}, \quad f_p \triangleq N\nu_p T_s = N\frac{\nu_p}{f_s}, \quad (4)$$

where N is the total number of samples in the sequence, the discrete-time input-output relation in (3) can be rewritten as

$$r[n] = \sum_{p=1}^P h_p e^{j2\pi f_p \frac{n}{N}} s[n - \ell_p] + w[n]. \quad (5)$$

Notice that the delay index ℓ_p represents the physical delay (in seconds) normalized by the sampling interval T_s , while the digital Doppler shift index f_p represents the physical Doppler shift (in Hz) normalized by the subcarrier spacing $\frac{f_s}{N}$. Therefore, depending on the channel scenario (i.e., the delay-Doppler profile) and the sampling frequency, the normalized indices ℓ_p and f_p may take either integer or fractional values, categorized into the following three cases:

Case 1: Integer Delay and Integer Doppler (IDID)

When both the normalized path delays and digital Doppler shifts are integer-valued, i.e., $\ell_p \in \mathbb{Z}_{\geq 0}$ and $f_p \in \mathbb{Z}$, the multipath components are perfectly aligned with the discrete sampling and frequency grids. For this case, here onwards referred to as integer-delay-integer-Doppler (IDID) channel, the discrete-time baseband received signal can be described by (5) directly without concern as ℓ_p is an integer, and therefore the shifted samples $s[n - \ell_p]$ are well-defined. Furthermore, the phase rotation term $e^{j2\pi f_p \frac{n}{N}}$ is an integer multiple of $e^{\frac{j2\pi}{N}}$, which corresponds to the fundamental frequency resolution of the discrete Fourier basis.

This is a common assumption adopted in most existing works, as it greatly simplifies the analysis and design of communication systems, reveals the core characteristics and behavior of each delay-Doppler tap without interference, and the associated complexity. However, such an assumption is often unrealistic in practical scenarios, where the delay and Doppler parameters are typically not perfectly aligned with the discrete grids, especially the Doppler shifts, necessitating more general models.

Case 2: Integer Delay and Fractional Doppler (IDFD)

In the integer-delay-fractional-Doppler (IDFD) case, the assumption of integer Doppler shifts is relaxed to reflect practical high-mobility environments better. Here, the normalized path delays remain integer-valued while the digital Doppler shifts are allowed to take non-integer (fractional) values, i.e., $\ell_p \in \mathbb{Z}_{\geq 0}$ and $f_p \in \mathbb{R}$. Note that the assumption of integer delays remains relatively robust, as the high sampling rate f_s provides a sufficiently fine resolution T_s to align multipath arrivals with the discrete grid.

In this case, the discrete-time model retains the structural form of (5), as the integer-shifted samples $s[n - \ell_p]$ are still aligned with the sampling instances. However, a critical distinction emerges in the phase rotation term $e^{j2\pi f_p \frac{n}{N}}$, where the Doppler shifts no longer correspond to integer multiples of the fundamental frequency resolution $e^{\frac{j2\pi}{N}}$. This misalignment breaks the periodic orthogonality of the discrete Fourier basis, the cornerstone of legacy waveforms such as OFDM, thereby introducing significant inter-carrier interference (ICI) and spectral leakage.

Case 3: Fractional Delay and Fractional Doppler (FDFD)

Finally, the FDFD model represents the most generalized and physically accurate case, where both the normalized delays and digital Doppler frequencies take arbitrary real values, i.e., $\ell_p \in \mathbb{R}_{\geq 0}$ and $f_p \in \mathbb{R}$. While integer delays are often acceptable in systems with moderate delays, fractional delays may become significant in ultra-high-precision synchronization and sensing applications.

In this case, the time-shifted argument $(n - \ell_p)$ in the transmit sequence is no longer strictly integer-valued. Consequently, the term $s[n - \ell_p]$ cannot be obtained by a simple index shift as in (5). This *fractionally delayed* version of the discrete sequence physically corresponds to the continuous-time signal being reconstructed from the discrete samples via a convolutional pulse-shaping filter $p(t)$, shifted by the continuous delay τ_p , and subsequently resampled at the receiver's sampling grid.

This process is mathematically expressed through a discrete-time interpolation¹, given by

$$s[n - \ell_p] = \sum_{m=0}^{N-1} s[m] g((n - m) - \ell_p), \quad (6)$$

where $g(\cdot)$ denotes the effective discrete-time pulse kernel, derived from the underlying pulse-shaping filter $p(t)$ such that $g(m) = p(mT_s)$, with sampling interval T_s .

Then, by substituting (6) into the discrete-time input-output relation in (3), we obtain the expanded discrete-time representation for a FDFD channel as

$$r[n] = \sum_{p=1}^P h_p e^{j2\pi f_p \frac{n}{N}} \sum_{m=0}^{N-1} s[m] g((n - m) - \ell_p) + w[n]. \quad (7)$$

¹Unlike idealized digital interpolation (e.g., sinc-based upsampling), which is independent of the waveform, the kernel $g(\cdot)$ in this model reflects the actual hardware pulse footprint (e.g., raised cosine or rectangular).

This formulation reveals that the choice of the physical pulse shape $p(t)$ directly governs the inter-sample coupling in the discrete domain. Consequently, this model provides a high-fidelity foundation that simultaneously accounts for spectral leakage due to fractional Doppler and the inter-sample interference caused by fractional delays, which is essential for evaluating next-generation waveforms in 6G propagation environments.

C. Generalized Matrix-form Input-Output Relationship

To facilitate efficient and insightful analysis, the discrete-time input-output relation for the FDFD channel in (7) can be equivalently expressed using a matrix-vector formulation. Namely, given a transmitted symbol block $\mathbf{s} \in \mathbb{C}^{N \times 1}$ of N samples, the received vector $\mathbf{r} \in \mathbb{C}^{N \times 1}$ is obtained under a circular convolution framework with a general prefix.

The signal sequence $s[n]$ is prepended with a prefix of length N_{cp} , described by

$$s[n'] = s[N+n'] \cdot e^{j2\pi\phi_{\text{cp}}(n')}, \forall n' \in \{-N_{\text{cp}}, \dots, -1\}, \quad (8)$$

where $\phi_{\text{cp}}(\cdot)$ is the waveform-dependent phase-offset function of the prefix samples, elaborated in Section III.

Given the above, the overall convolution matrix $\mathbf{H} \in \mathbb{C}^{N \times N}$ represents the doubly dispersive channel as

$$\mathbf{r} = \mathbf{H}\mathbf{s} + \mathbf{w} = \sum_{p=1}^P h_p \mathbf{H}_p \mathbf{s} + \mathbf{w}, \quad (9)$$

where $h_p \in \mathbb{C}$ denotes the complex path gain of the p -th multipath component, identical to that of (1), (3), and (7), \mathbf{H}_p is the circular convolutional matrix excluding the path gain coefficient h_p for the p -th path, $\mathbf{r} \in \mathbb{C}^{N \times 1}$ is the received signal vector collecting the N useful samples of $r[n]$ after discarding the prefix, and $\mathbf{w} \in \mathbb{C}^{N \times 1}$ represents the noise received per sample.

For the IDID and IDFD cases, where the normalized delays ℓ_p are integer-valued, the per-path channel matrix \mathbf{H}_p can be decomposed as the product of a diagonal phase-rotation matrix and a cyclic permutation matrix, yielding [16], [28], [29], [51], [67]

$$\mathbf{H}_p = \Phi_p \cdot \mathbf{V}^{f_p} \cdot \Pi^{\ell_p} \in \mathbb{C}^{N \times N}. \quad (10)$$

The three matrix components in (10) are, respectively:

1) diagonal phase-offset matrix Φ_p , which models the phase-offset of the utilized prefix in (8) as

$$\Phi_p \triangleq \text{diag}(\phi_p) \in \mathbb{C}^{N \times N} \quad (11)$$

$$= \text{diag}\left(\underbrace{[e^{-j2\pi\phi_{\text{cp}}(\ell_p)}, \dots, e^{-j2\pi\phi_{\text{cp}}(1)}]}_{\ell_p \text{ terms}}, \underbrace{[1, \dots, 1]}_{N-\ell_p \text{ ones}}\right);$$

2) diagonal Doppler shift matrix \mathbf{V}^{f_p} , which models the effect of the normalized digital Doppler shifts f_p based the N -th roots-of-unity matrix

$$\mathbf{V} \triangleq \text{diag}(\mathbf{v}) \in \mathbb{C}^{N \times N} \quad (12)$$

$$= \text{diag}\left([1, e^{-j2\pi\frac{1}{N}}, \dots, e^{-j2\pi\frac{N-1}{N}}]\right),$$

which when raised to the f_p -th power as \mathbf{V}^{f_p} , is the diagonal matrix representing the phase rotation due to the Doppler shift; and

3) forward cyclic shift matrix Π^{ℓ_p} , which models the **integer** delay shift of ℓ_p samples, defined based on the single-step forward cyclic shift matrix Π

$$\Pi = \begin{bmatrix} 0 & 0 & \cdots & 0 & 1 \\ 1 & 0 & \cdots & 0 & 0 \\ 0 & 1 & \ddots & \vdots & \vdots \\ \vdots & \ddots & \ddots & 0 & 0 \\ 0 & \cdots & 0 & 1 & 0 \end{bmatrix} \in \mathbb{C}^{N \times N}, \quad (13)$$

such that left-multiplying a vector by Π , i.e., $\Pi\mathbf{x}$, corresponds to a forward shift of \mathbf{x} , and therefore Π^{ℓ_p} corresponds to a cyclic forward shift of ℓ_p indices.

As can be seen with the above formulation, the IDID and IDFD cases benefit from a highly sparse channel matrix \mathbf{H}_p , which consists of only a single non-zero element per row and column, due to the perfect alignment of the delays ℓ_p with the sampling grid (diagonal phase matrices and permutation matrix structure).

However, in the FDFD case with **non-integer** delays ℓ_p , it can be observed that such efficient formulations in (11) and (13) based on integer delays ℓ_p are no longer valid - in a similar construction to (7).

Namely, the separation of the phase-offset matrix and the shift matrix into independent diagonal and permutation operators Φ_p and Π^{ℓ_p} is no longer possible due to the inter-sample interference caused by fractional delays and the effective discrete-time pulse kernel $g(\cdot)$, and the generalized per-path FDFD channel matrix can be expressed as

$$\mathbf{H}_p \triangleq \mathbf{V}^{f_p} \cdot \Psi(\ell_p) \in \mathbb{C}^{N \times N}, \quad (14)$$

where \mathbf{V}^{f_p} models the sample-wise phase rotations due to the digital Doppler shift f_p - identical to the IDID and IDFD cases, while the new *chirp-periodically circulant* fractional delay matrix $\Psi(\ell_p)$ captures the combined effect of the fractional delay and the corresponding prefix phase-offset, defined as

$$\Psi(\ell_p) \triangleq (\mathbf{G}(\ell_p) + \Phi(\ell_p)) \in \mathbb{C}^{N \times N}, \quad (15)$$

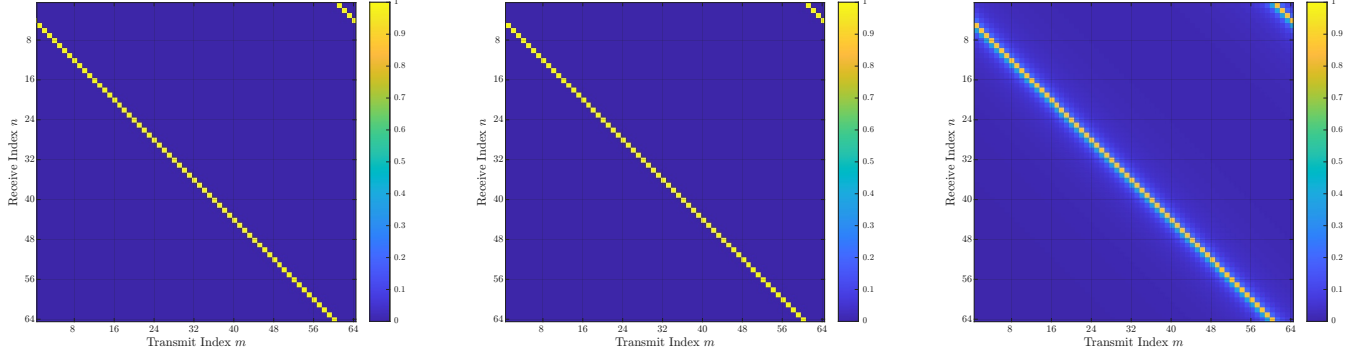
with the constituting effective interpolated delay matrix $\mathbf{G}(\ell_p)$ and the effective interpolated delay chirp-periodic prefix (CPP) matrix $\Phi_p(\ell_p)$ defined element-wise as

$$[\mathbf{G}(\ell_p)]_{n,m} = g(n - m - \ell_p), \quad (16)$$

$$[\Phi(\ell_p)]_{n,m} = g(n - m - \ell_p + N) \cdot e^{j2\pi\phi_{\text{cp}}(n-m-\ell_p)}, \quad (17)$$

where $\mathbf{G}(\ell_p)$ is generally dense and Toeplitz.

As illustrated in Fig. 1, for integer delays, the sum $\mathbf{G}(\ell_p) + \Phi_p(\ell_p)$ perfectly reconstructs the sparse, phase-rotated cyclic permutation matrix used in legacy OFDM and AFDM literature, as evidenced by the identity between Fig. 1(a) – based on (10), and Fig. 1(b) – based on (14) and (15).

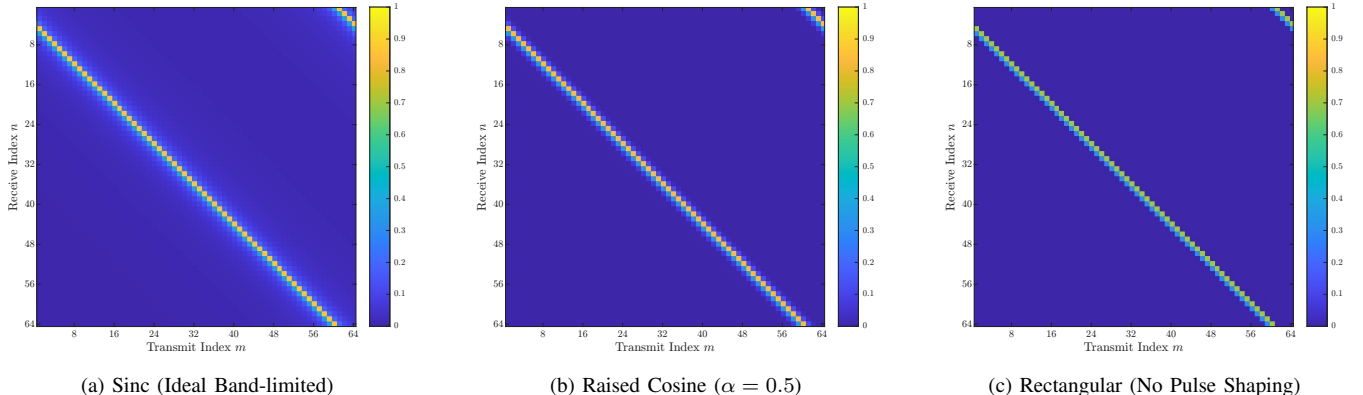


(a) Conventional IDID model following (10).

(b) Generalized IDID model following (14).

(c) Generalized FDFD model following (14).

FIGURE 1: Illustration of a single path within the channel matrix under IDID and FDFD scenarios, with $N = 64$. (a) shows the conventional IDID sparse permutation model of eq. (10) with $\ell_p = 4$ and $f_p = 2$; (b) shows the proposed generalized FDFD formulation of eq. (14) but under the same integer conditions; and (c) shows the proposed generalized FDFD formulation with fractional delay ($\ell_p = 4.3$) and fractional Doppler ($f_p = 2.1$), revealing the inter-sample coupling effects. The FDFD models in (b) and (c) are constructed based on the ideal band-limited pulse (Sinc interpolation).



(a) Sinc (Ideal Band-limited)

(b) Raised Cosine ($\alpha = 0.5$)

(c) Rectangular (No Pulse Shaping)

FIGURE 2: Impact of different transmit pulse shapes $g(\cdot)$ on the single-path FDFD channel matrix \mathbf{H}_p ($N = 64$, $\ell_p = 4.3$, $f_p = 2.1$), where the choice of the transmit filter governs the sparsity of the inter-sample coupling and the thickness of the diagonal band, while the main position of the shifted components remains unchanged and deterministic to the integer delay part $\lfloor \ell_p \rfloor$.

Furthermore, the introduction of fractional delays in Fig. 1(c) reveals the dense inter-sample coupling inherent to true 6G doubly dispersive channels², where each received sample becomes a linear combination of all N transmitted samples.

This framework inherently therefore accommodates the transmit pulse-shape's influence on channel coupling, where the pulse-shape kernel $g(\cdot)$ affects inter-sample coupling. Under the ideal band-limited assumption (sinc interpolation kernel), the channel matrix exhibits the true inter-sample smearing and a consequently denser structure, distributing symbol energy across a wide band diagonal. In contrast, a rectangular pulse (non-pulse-shaped) yields a significantly sparser matrix with minimal inter-sample coupling, albeit with non-ideal spectral leakage and ICI. In between, a practical raised cosine pulse achieves better localization than the sinc kernel while capturing sufficient inter-sample coupling, and still obtains a sufficiently sparse structure exploitable for efficient estimation and detection algorithms.

D. Extension to MIMO Channels

The above SISO formulation can be generalized to MIMO scenarios with N_t transmit and N_r receive antennas. The time-delay domain time-varying impulse response between transmit antenna n_t and receive antenna n_r , where $n_t \in \{1, \dots, N_t\}$ and $n_r \in \{1, \dots, N_r\}$, is expressed as

$$h_{n_r, n_t}(t, \tau) \triangleq \sum_{p=1}^P h_p e^{j2\pi\nu_p t} e^{j2\pi(\psi_r(n_r, \theta_p^r) + \psi_t(n_t, \theta_p^t))} \delta(\tau - \tau_p), \quad (18)$$

where θ_p^t and θ_p^r represent the angle-of-departure (AoD) and angle-of-arrival (AoA) of the p -th path, respectively, and h_p , τ_p , and ν_p are the path gain, delay, and Doppler shift, and the phase progression terms $\psi_t(\cdot)$ and $\psi_r(\cdot)$ are defined as

$$\psi_t(n_t, \theta_p^t) = \frac{d_t(n_t-1)}{\lambda_c} \sin(\theta_p^t), \quad (19)$$

$$\psi_r(n_r, \theta_p^r) = \frac{d_r(n_r-1)}{\lambda_c} \sin(\theta_p^r), \quad (20)$$

where d_t and d_r denote the inter-element spacings at the transmit and receive arrays, and λ_c is the carrier wavelength.

²The proposed core FDFD channel model is readily extensible to broader doubly-dispersive channel scenarios [68]–[71].

Following the sampling procedure in Section B and the FDFD case, the discrete-time baseband channel between the n_t -th transmit and n_r -th receive antennas can be written as

$$r_{n_r}[n] = \sum_{n_t=1}^{n_t} \left(\sum_{p=1}^P h_p e^{j2\pi f_p \frac{n}{N}} e^{j2\pi (\psi_r(n_r, \theta_p^r) + \psi_t(n_t, \theta_p^t))} \right. \\ \left. \times \sum_{m=0}^{N-1} s_{n_t}[m] g((n-m) - \ell_p) \right) + w_{n_r}[n], \quad (21)$$

where f_p and ℓ_p are the normalized digital Doppler and delay indices, respectively, and $w_{n_r}[n]$ denotes the AWGN term with $w_{n_r}[n] \sim \mathcal{CN}(0, \sigma_w^2)$.

Furthermore, to express the spatial dependence compactly, we define the transmit and receive array response vectors of the p -th path as

$$\mathbf{a}_t(\theta_p^t) \triangleq \left[e^{j2\pi\psi_t(1, \theta_p^t)}, \dots, e^{j2\pi\psi_t(N_t, \theta_p^t)} \right]^T \in \mathbb{C}^{N_t \times 1}, \quad (22)$$

$$\mathbf{a}_r(\theta_p^r) \triangleq \left[e^{j2\pi\psi_r(1, \theta_p^r)}, \dots, e^{j2\pi\psi_r(N_r, \theta_p^r)} \right]^T \in \mathbb{C}^{N_r \times 1}. \quad (23)$$

Then, the per-path MIMO channel between all transmit and receive antennas can be expressed by the outer product of the array response vectors, defined as

$$\Theta_p \triangleq \mathbf{a}_r(\theta_p^r) \cdot \mathbf{a}_t^H(\theta_p^t) \in \mathbb{C}^{N_r \times N_t}, \quad (24)$$

which captures the spatial signature of the p -th path.

Then, stacking the transmit signal samples at the n -th index across N_t antennas as $\mathbf{s}[n] = [s_1[n], s_2[n], \dots, s_{N_t}[n]]^T \in \mathbb{C}^{N_t \times 1}$ and the received samples as $\mathbf{r}[n] = [r_1[n], r_2[n], \dots, r_{N_r}[n]]^T \in \mathbb{C}^{N_r \times 1}$, the general discrete-time FDFD MIMO input-output relation becomes

$$\mathbf{r}[n] = \sum_{p=1}^P h_p e^{j2\pi f_p \frac{n}{N}} \cdot \Theta_p \cdot \sum_{m=0}^{N-1} \mathbf{s}[m] g((n-m) - \ell_p) + \mathbf{w}[n], \quad (25)$$

where $\mathbf{w}[n] \in \mathbb{C}^{N_r \times 1}$ denotes the receive noise vector.

Finally, by stacking the N sample vectors into $\bar{\mathbf{r}} \in \mathbb{C}^{N_r N \times 1}$ and the corresponding transmitted samples into $\bar{\mathbf{s}} \in \mathbb{C}^{N_t N \times 1}$, the overall blockwise discrete-time MIMO FDFD model can be compactly represented as

$$\bar{\mathbf{r}} = \left(\sum_{p=1}^P h_p \cdot \Theta_p \otimes \left(\mathbf{V}^{f_p} \cdot \Psi(\ell_p) \right) \right) \cdot \bar{\mathbf{s}} + \bar{\mathbf{w}} \quad (26)$$

where \otimes denotes the Kronecker product, and $\Psi(\ell_p) \in \mathbb{C}^{N \times N}$ and $\mathbf{V}^{f_p} \in \mathbb{C}^{N \times N}$ represent as defined in the FDFD SISO system model in (14).

Similarly, this uniform linear array (ULA) model can be extended to other array geometries, such as uniform planar arrays (UPAs) and non-uniform arrays, by appropriately extending and modifying the array response vectors, but is omitted from the scope of this article.

III. On the Compatibility of AFDM over OFDM

In this next section, we examine the AFDM modulator and demodulator structures in detail and show that it requires virtually no modifications to the underlying hardware architecture relative to legacy OFDM, particularly for the core transform processing, pulse shaping, resource allocation, and prefixing. All conventional OFDM modulator blocks can be reused directly, with only minimal additions in baseband processing.

To that end, let us first introduce the input-output system model of the conventional OFDM and the AFDM modulator/demodulator, given the model of the discrete-time doubly dispersive channel in Section B.

A. OFDM Signal Model

Let the k -th data symbol be denoted by $x_k \in \mathcal{X}$ for $k \in \{0, \dots, N-1\}$, where $\mathcal{X} \subset \mathbb{C}$ is the complex constellation set, with cardinality $|\mathcal{X}| = M$, i.e., M -QAM or M -PSK.

Then, the OFDM transmit signal block with N samples in the time domain is generated via the inverse discrete Fourier transform (IDFT) as $\mathbf{s} = \mathbf{F}^H \cdot \mathbf{x} \in \mathbb{C}^{N \times 1}$, where $\mathbf{s} \in \mathbb{C}^{N \times 1}$ is the transmit signal vector collecting one OFDM block in the time domain, $\mathbf{x} = [x_0, x_1, \dots, x_{N-1}]^T \in \mathbb{C}^{N \times 1}$ is the vector collecting the N data symbols, and $\mathbf{F} \in \mathbb{C}^{N \times N}$ is the normalized N -point discrete Fourier transform (DFT) matrix.

For OFDM, the prefix required is a cyclic prefix (CP), and does not need a phase-offset per sample, and therefore, $\phi_{cp}(\cdot) = 0$ and $\Psi(\ell_p) = \mathbf{G}(\ell_p)$ in (15), yielding

$$\mathbf{r} = \left(\sum_{p=1}^P h_p \cdot \mathbf{V}^{f_p} \cdot \mathbf{G}(\ell_p) \right) \mathbf{F}^H \cdot \mathbf{x} + \mathbf{w} \in \mathbb{C}^{N \times 1}. \quad (27)$$

On the receiver side, the OFDM demodulator applies the forward N -point normalized DFT to the received signal, yielding the frequency-domain received vector as

$$\mathbf{y} = \mathbf{F} \cdot \mathbf{r} = \mathbf{F} \left(\underbrace{\sum_{p=1}^P h_p \cdot \mathbf{V}^{f_p} \cdot \mathbf{G}(\ell_p)}_{\triangleq \mathbf{\Xi}_{\text{OFDM}} \in \mathbb{C}^{N \times N}} \right) \mathbf{F}^H \cdot \mathbf{x} + \mathbf{F} \mathbf{w} \in \mathbb{C}^{N \times 1}, \quad (28)$$

where, since the modulator and demodulator are independent of the path index p , the effective channel matrix describing the input-output relation of the data symbols can be expressed as the sum of the per-path effective channels, as

$$\mathbf{\Xi}_{\text{OFDM}} \triangleq \sum_{p=1}^P h_p \cdot \mathbf{\Xi}_p^{\text{OFDM}} \in \mathbb{C}^{N \times N}, \quad (29)$$

with $\mathbf{\Xi}_p^{\text{OFDM}} \triangleq \mathbf{F} \cdot \mathbf{V}^{f_p} \cdot \mathbf{G}(\ell_p) \cdot \mathbf{F}^H \in \mathbb{C}^{N \times N}$.

One may see that with integer delays and no Doppler shift, i.e., $\mathbf{G}(\ell_p) = \mathbf{\Pi}^{\ell_p}$ and $\mathbf{V}^{f_p} = \mathbf{I}_N$, the effective channel matrix reduces to a completely diagonal matrix, which preserves the orthogonality among subcarriers and avoids inter-carrier interference – the defining characteristic of OFDM in static multipath channels.

However, when Doppler shifts are present, it is well known that the orthogonality among OFDM subcarriers is disrupted, leading to ICI. This effect is observed in the above model with the presence of $\mathbf{V}^{f_p} \neq \mathbf{I}_N$ introducing phase-rotations in the subcarriers, which no longer align with the Fourier basis. Therefore, off-diagonal elements appear in the effective channel matrix even when f_p is integer-valued, which are indistinguishable between paths.

For fractional Doppler or delay values, the interference becomes more severe, and the effective channel becomes extremely dense, further increasing interference.

B. AFDM Signal Model

To address the challenges posed by Doppler shifts identified above, the AFDM was proposed to convert the static subcarriers of OFDM into chirp-based subcarriers in the discrete affine Fourier transform (DAFT) basis.

The AFDM transmit block with N samples in the time domain is generated via the inverse discrete affine Fourier transform (IDAFT) as

$$\mathbf{s} = \mathbf{A}^H \cdot \mathbf{x} \in \mathbb{C}^{N \times 1}, \quad (30)$$

where $\mathbf{A} \in \mathbb{C}^{N \times N}$ is the forward normalized DAFT matrix, which is unitary, described by

$$\mathbf{A} \triangleq \Lambda_{\lambda_2} \mathbf{F}_N \Lambda_{\lambda_1} \in \mathbb{C}^{N \times N}, \quad (31)$$

where $\mathbf{F}_N \in \mathbb{C}^{N \times N}$ is the N -point DFT matrix, and $\Lambda_{\lambda_i} \triangleq \text{diag}[e^{-j2\pi\lambda_i(0)^2}, \dots, e^{-j2\pi\lambda_i(N-1)^2}] \in \mathbb{C}^{N \times N}$ is a diagonal chirp matrix defined by a central digital frequency λ_i , with two parametrizable chirp parameters λ_1 and λ_2 .

Note that setting $\lambda_1 = \lambda_2 = 0$ yields the standard DFT, while $\lambda_1 = \lambda_2 = \frac{1}{2N}$ corresponds to the discrete Fresnel transform matrix utilized in orthogonal chirp division multiplexing (OCDM). Furthermore, the first chirp frequency λ_1 is a crucial parameter which can be optimized based on the channel statistics to enhance performance under doubly dispersive channels and ensure full diversity, namely to satisfy [28], [29]

$$\lambda_1 \geq \frac{2(f_{\max} + \xi) + 1}{2N}, \quad (32)$$

where $\lfloor f_{\max} \rfloor \in \mathbb{Z}^+$ is the closest integer value of the maximum normalized Doppler shift f_{\max} , and $\xi \in \mathbb{Z}^+$ is a design parameter typically referred to as the *guard width* that provides a margin for robustness in Doppler.

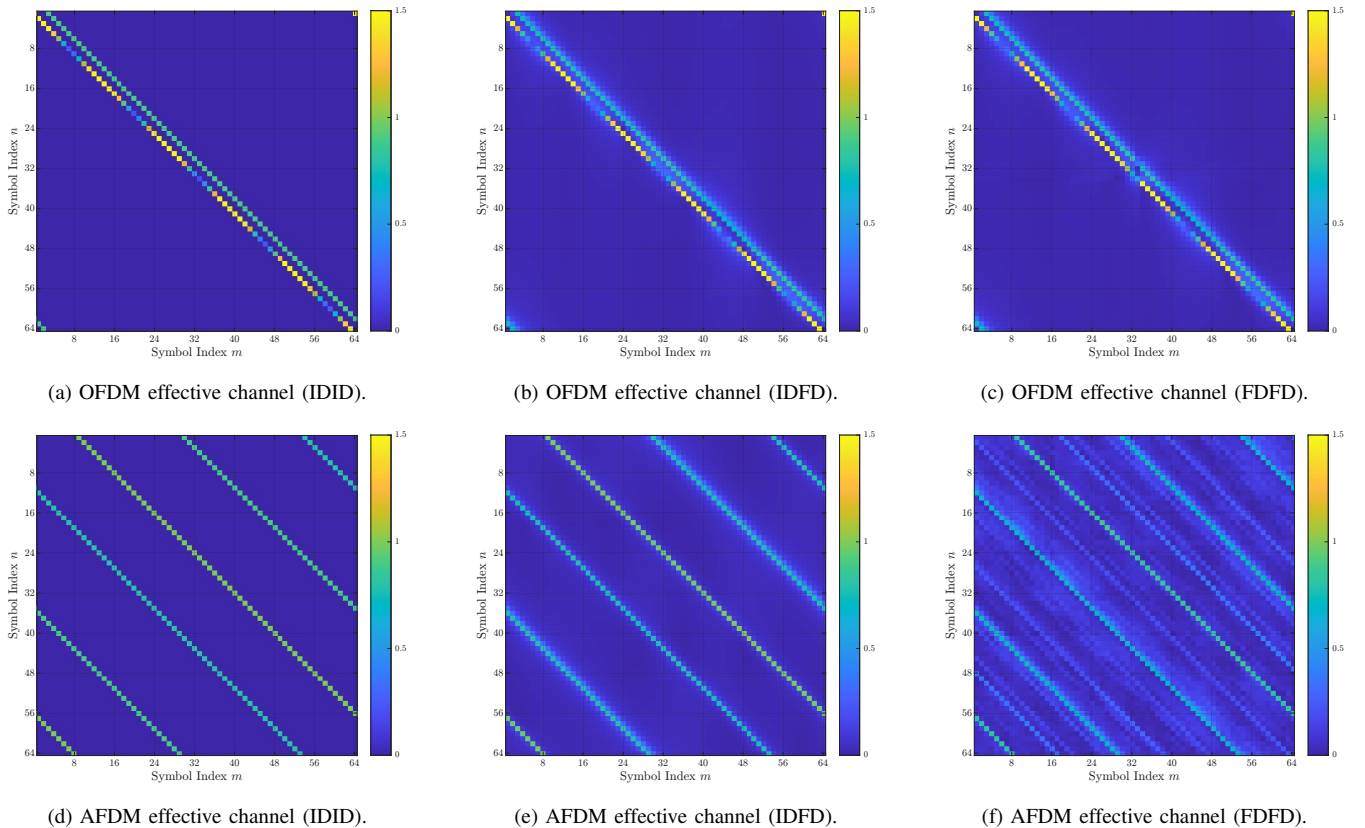


FIGURE 3: Effective channel matrices Ξ for OFDM and AFDM, respectively on the first and second rows, in a 3-path doubly dispersive scenario with $N = 64$. The physical channel parameters are defined by path coefficients $\{1, 0.9, 0.8\}$, normalized delays $\{1.3, 3.25, 5.96\}$, and normalized digital Dopplers $\{1.1, -2.3, 0.85\}$, where for the IDID and IDFD cases, the delays and Dopplers are rounded to the nearest integers as relevant. For the AFDM implementation, chirp parameters are set to $c_1 = (2(f_{\max} + 1) + 1)/2N$, with $f_{\max} = 3$, and $c_2 = 1/2N$. It can be seen that on top of the discussed effects of the fraction taps in Section II-C, the different paths of the OFDM effective channel matrices are indistinguishable under Doppler shifts, leading to significant inter-carrier interference, while AFDM maintains a more distinguishable effective channel matrix, preserving better orthogonality.

On the other hand, the second chirp parameter λ_2 does not influence the orthogonality of AFDM over doubly dispersive channels. Instead, it serves as a flexible degree of freedom for tailoring time-domain waveform properties, such as the ambiguity function and PAPR characteristics.

To prevent spectral aliasing and ensure a unique signal representation, λ_2 is typically chosen such that $\lambda_2 \ll 1$ or $\lambda_2 \in \mathbb{R} \setminus \mathbb{Q}$ (*i.e.*, an irrational value), to ensure that the phase progression of the second chirp does not periodically align with the discrete sampling grid. Given the above, the necessary prefix in AFDM is a CPP to ensure circular convolution under chirp-domain periodicity, determined by the phase-offset function $\phi_{\text{cp}}^{\text{AFDM}}(n) = \lambda_1(N^2 + 2Nn)$, making Φ_p in (11) non-identity.

However, it is also known that for specific configurations of the AFDM parameters, namely when $2N\lambda_1$ is an even integer, the CPP reduces to a conventional cyclic prefix (CP) without phase offsets, *i.e.*, $\phi_{\text{cp}}^{\text{AFDM}}(n) = 0$ for all n , and therefore $\Phi_p = \mathbf{I}_N$.

Given the above, the received signal after passing through the doubly dispersive channel in the general FDFD case is expressed as

$$\mathbf{r} = \left(\sum_{p=1}^P h_p \cdot \Phi_p \cdot \mathbf{V}^{f_p} \cdot \mathbf{G}(\ell_p) \right) \mathbf{A}^H \cdot \mathbf{x} + \mathbf{w} \in \mathbb{C}^{N \times 1}. \quad (33)$$

At the receiver, the demodulator applies the matched forward DAFT, *i.e.*, with the same parametrization of λ_1 and λ_2 , yielding the received vector $\mathbf{y} = \mathbf{A} \cdot \mathbf{r}$ in the affine-frequency domain as

$$\mathbf{y} = \mathbf{A} \left(\sum_{p=1}^P h_p \cdot \Phi_p \cdot \mathbf{V}^{f_p} \cdot \mathbf{G}(\ell_p) \right) \mathbf{A}^H \cdot \mathbf{x} + \mathbf{A} \mathbf{w} \quad (34)$$

with $\Xi^{\text{AFDM}} \triangleq \sum_{p=1}^P h_p \cdot \Xi_p^{\text{AFDM}}$, where Ξ^{AFDM} represents the structural effective channel matrix describing the input-output relation of the data symbols between the AFDM modulator and demodulator, which, as in the OFDM case, can be expressed as the sum of the per-path components and the channel fading coefficients, with $\Xi_p^{\text{AFDM}} \triangleq \mathbf{A} \cdot \Phi_p \cdot \mathbf{V}^{f_p} \cdot \mathbf{G}(\ell_p) \cdot \mathbf{A}^H \in \mathbb{C}^{N \times N}$.

The OFDM and AFDM effective channels have been illustrated for the IDID, IDFD, and FDFD cases in Fig. 3.

C. MIMO Extension of OFDM and AFDM Signal Models

Given the above, the MIMO signal model of OFDM and AFDM can be easily obtained by a block-wise application of the modulator and the demodulator to a stacked model, which translates to replacing the SISO channel part in (26) with the effective channel model including the modulator operations, *i.e.*,

$$\bar{\mathbf{y}}^{\text{MIMO-OFDM}} = \left(\sum_{p=1}^P h_p \cdot \Theta_p \otimes \Xi_p^{\text{OFDM}} \right) \bar{\mathbf{x}} + \tilde{\mathbf{w}}, \quad (35)$$

$$\bar{\mathbf{y}}^{\text{MIMO-AFDM}} = \left(\sum_{p=1}^P h_p \cdot \Theta_p \otimes \Xi_p^{\text{AFDM}} \right) \bar{\mathbf{x}} + \tilde{\mathbf{w}}. \quad (36)$$

Trivially, the channel structure exhibits the same per-block interference characteristics as in the SISO case, but with the corresponding antenna response coefficients across antennas.

D. A Note on OFDM and AFDM Compatibility

For the modulator/demodulator, the fundamental DAFT/IDAFT steps only require a core FFT/IFFT block, and two subcarrier-wise (element-wise) phase rotation blocks, as also described in (31), and therefore for any parametrization of the AFDM, its modulator/demodulator requires these two phase-rotation blocks (highlighted in blue), placed immediately before and after the FFT/IFFT block (highlighted in green), as illustrated in Fig. 4. Most importantly, this very phase-rotation mechanism is not foreign to conventional OFDM implementations, and in fact, already a widely adopted operation in existing systems and techniques, such as: the *Selected Mapping (SLM)* method for PAPR reduction, where each OFDM symbol is multiplied by a unit-magnitude phase vector before the IFFT [72], the *Cyclic Delay Diversity (CDD)* technique adopted in LTE, where transmit antennas apply linearly varying per-subcarrier phase rotations to achieve frequency diversity [73], *pilot phase randomization* in IEEE 802.11 WLANs, where predefined phase sequences modulate pilot subcarriers to aid carrier tracking [74], and *pilot scrambling* in DBV-T, where pilot tones are multiplied by a pseudo-random binary phase to reduce interference [75].

Furthermore, the remaining baseband processing blocks, such as resource mapping for pilots and subcarrier allocation, can be directly reused, since the resources in AFDM are indexed in a one-dimensional (affine) frequency domain. Similarly, the prefix is also directly prepended along this single dimension, followed by a time-domain windowing block, which can be applied directly in the time-domain identically to that of conventional OFDM. In summary, AFDM does not require any changes to the physical transceiver hardware, introducing only lightweight baseband chirp rotations and CPP phase adjustments.

This high level of structural compatibility between AFDM and OFDM contrasts with OTFS, which requires few fundamentally different modulator structures. The OTFS waveform is inherently defined in the delay-Doppler domain and relies on either an inverse symplectic finite Fourier transform (ISFFT) combined with the Heisenberg transform (HT), or the inverse discrete Zak transform (IDZT), to transform the delay-Doppler symbols into a time-domain sequence. When assuming the non-ideal rectangular pulses for interpolation and upsampling, this combination of ISFFT and HT collapses into the IDZT, which can be efficiently implemented using interleavers and multiple lower-dimensional IDFTs. However, in practical doubly dispersive channels with non-integer Dopplers and delays, the necessary bi-orthogonality property of the OTFS basis are not fully satisfied under such non-ideal rectangular pulses, and therefore complex pulse-shaping is necessary as will be further elaborated in the following.

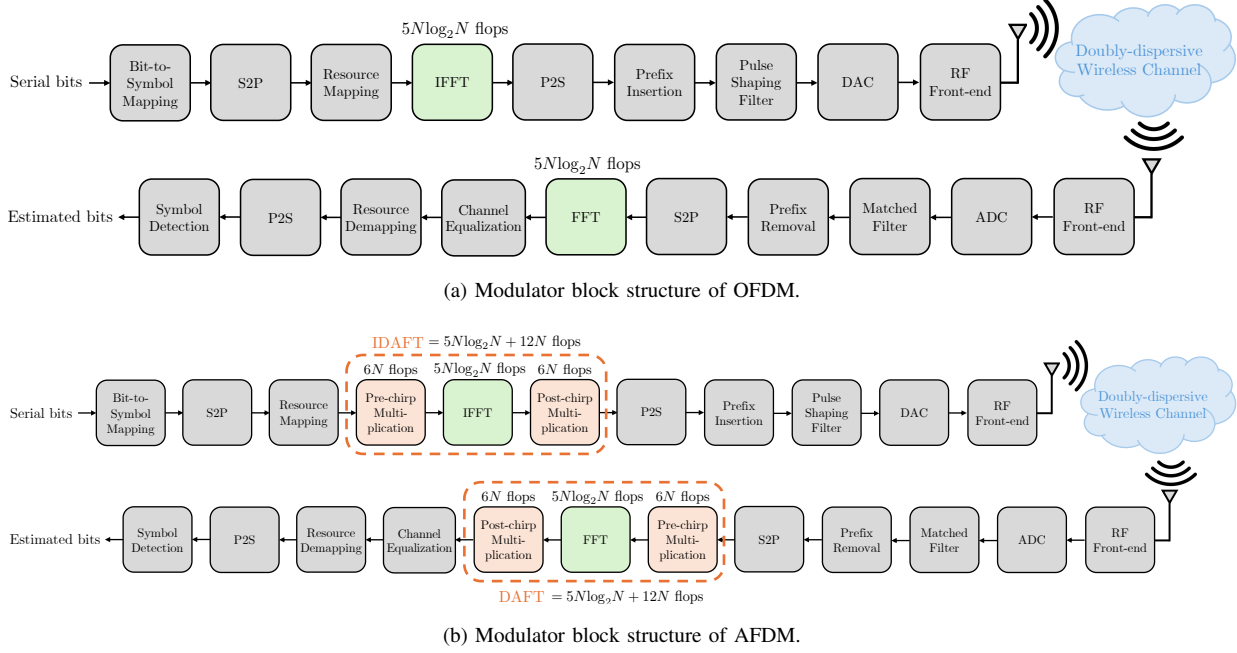


FIGURE 4: Comparison of OFDM and AFDM transceiver structures, which highlights that the only structural difference lies in the two element-wise chirp-phase rotations (pre- and post-multiplications) surrounding the IFFT/FFT blocks from the conventional OFDM transceivers.

E. Pulse-Shaping, Windowing, and Prefixing Blocks

Indeed, pulse-shaping is an important criteria in the discrete-time modeling and practical realization of multicarrier waveforms in doubly dispersive channels. The legacy OFDM systems (e.g., LTE, 5G NR, Wi-Fi) traditionally employ an implicit rectangular pulse (i.e., no pulse-shaping) alongside a cyclic prefix which still ensures orthogonality in static multipath channels, but in a general case additional spectral containment may be desired, especially under high-mobility channels, which is implemented by a time-domain windowing framework (sometimes also simply called OFDM pulse-shaping), where a real-valued filter is applied sample-wise prior to the digital-to-analog conversion (DAC), i.e.,

$$\mathbf{s}_{ps} = \text{diag}(\mathbf{p}) \cdot \mathbf{s}_{cp} = \mathbf{p} \odot \mathbf{s}_{cp} \in \mathbb{C}^{(N+N_{cp}) \times 1}, \quad (37)$$

where $\mathbf{s}_{cp} \in \mathbb{C}^{(N+N_{cp}) \times 1}$ is the modulator output vector including a cyclic prefix of length N_{cp} , and $\mathbf{p} \in \mathbb{R}^{(N+N_{cp}) \times 1}$ is the real-valued windowing filter, and $\mathbf{s}_{ps} \in \mathbb{C}^{(N+N_{cp}) \times 1}$ is the windowed transmit signal vector.

For the AFDM, the modulator and demodulator architecture admit the same generic pulse-shaping operation without altering hardware, employing the same digital filter in (37) as OFDM prior to transmission, as the subcarrier orthogonality in time-frequency domain is guaranteed by the underlying unitary basis function DAFT and the CPP ensures circular convolutional structure under chirp-periodicity, just as the OFDM's DFT basis with CP, although some non-ideal spectral properties may arise [76].

However, as briefly mentioned before, the more critical result is for the OTFS, where the theoretically ideal

bi-orthogonality property of OTFS in delay-Doppler can not be fully satisfied in practical systems with finite signal support, especially under rectangular pulses. In such cases, the practical OTFS input-output relation departs from the theoretical delay-Doppler convolution model, and OTFS suffers from loss of bi-orthogonality, necessitating complex equalization. Therefore, OTFS absolutely requires dedicated pulse-shaping in the interpolating upsampler to restore the loss of bi-orthogonality (which can never be exact, only approach very close to the theoretical), a limitation not present in OFDM and AFDM whose channel and modulation basis remain mutually orthogonal for arbitrary pulse shapes.

One approach of pulse shaping for OTFS is to apply a time-domain pulse-shaping HT after the ISFFT, which can mitigate some non-idealities but remains fundamentally limited by finite support and the Balian-Low constraints. However, the non-rectangular pulse-shaping HT implies that the OTFS modulator requires three consecutive FFT/IFFT operations with interleaving and reshaping, which cannot be reduced further as commonly assumed for the rectangular pulse case, leading to increase in complexity and latency.

Alternatively, recent work on Zak-OTFS introduces a direct delay-Doppler domain pulse-shaping approach, which eliminates the need for the ISFFT and HT, but instead requires a two-dimensional convolution in the delay-Doppler domain for the pulse shaping before the single IDZT. This DD-domain filtering enables more controlled localization and yields the closest practical approximation to the ideal twisted convolution, although perfect bi-orthogonality remains unattainable under finite time-bandwidth constraints.

Thus, careful pulse shaping is necessary for OTFS to retain its desired structural characteristics in practical doubly-dispersive channels, whereas AFDM and OFDM preserve their orthogonality and convolutional forms even with simple rectangular pulses.

Furthermore, unlike AFDM, where a one-dimensional cyclic prefix (with chirp periodicity) is sufficient to ensure robustness, OTFS has recently been shown to require a so-called double cyclic prefix (in both time and frequency dimensions) to improve its robustness on top of the single time-domain cyclic prefix [77], [78]. This unique prefixing strategy necessitates a distinct resource allocation and indexing scheme, and also leads to increased signaling overhead and complexity.

Overall, this section shows that AFDM preserves the core OFDM hardware pipeline and one-dimensional framing structure, requiring only lightweight digital chirp rotations and a re-parameterized cyclic prefix, without introducing new baseband modules or RF redesign. In contrast, OTFS relies on a fundamentally different modulation domain, multi-stage 2D transform processing, and non-native prefixing and resource grids, leading to substantial transceiver and standardization divergence. Consequently, AFDM emerges as a hardware- and specification-efficient evolutionary waveform candidate for next-generation systems.

IV. Analysis of the AFDM Transceiver over OFDM

A. Modulation Complexity and Scalability

Drawing from the previous section, the additional computational burden introduced by the AFDM modulator/demodulator, relative to conventional OFDM, stems only from the two chirp-domain element-wise phase rotation operations applied immediately before and after the FFT/IFFT stage, as all other operations and blocks are identical and can be reused directly (excluding the channel equalization block), as shown in Fig. 4. Thereby, each complex phase rotation over N samples (equivalent to the number of subcarriers) is implemented simply via N element-wise complex multiplications, which require a total of $6N$ floating point operations (FLOPs). Hence, the two rotations introduce an extra cost of $12N$ FLOPs per AFDM symbol block of N complex symbols.

With the conventional Q -point FFT/IFFT cost given by $C_{FFT,Q} \triangleq 5Q \log_2 Q$ FLOPs, the total per-block modulator/demodulator complexity for AFDM with N symbols is then obtained as

$$C_{AFDM,N} = 5N \log_2 N + 12N \quad [\text{FLOPs}] \quad (38)$$

By comparison, the conventional OFDM modulator cost is trivially given by the complexity of the N -point IFFT/FFT blocks directly, i.e., $C_{OFDM,N} = C_{FFT,N} + 2N$. Therefore, the relative complexity overhead of AFDM over OFDM is

$$\frac{C_{AFDM,N} - C_{OFDM,N}}{C_{OFDM,N}} = \frac{12N}{5N \log_2 N} = \frac{12}{5 \log_2 N} \quad (39)$$

For practical FFT/IFFT sizes (number of subcarriers) considered in 6G, the overhead in (39) evaluates to modest values, with $N = 256$ amounting to a 30% overhead, $N = 1024$ to 24%, and $N = 4096$ to 20%. Hence, while the chirp rotations are not cost-free nor negligible, their asymptotic impact logarithmically diminishes with growing number of subcarriers, which promotes their scalability, and the dominant complexity term remains the FFT/IFFT.

Next, as a reference and comparison, we provide a similar analysis for the OTFS. For the ISFFT + HT approach with the OTFS delay-Doppler frame of size $K \times L$, where we set $N = KL$ to fairly compare the different waveforms in terms of the resource usage (i.e., number of discrete symbol resources), the total complexity of the ISFFT, which is implemented using L IFFTs of size K , and K FFTs of size L , is given by

$$\begin{aligned} C_{ISFFT,KL} &= L(5K \log_2 K) + K(5L \log_2 L) \quad [\text{FLOPs}] \\ &= 5KL(\log_2 KL) = 5N \log_2 N = C_{FFT,N}, \end{aligned} \quad (40)$$

i.e., the same as a single N -point IFFT for $N = KL$.

Then, a pulse-shaped HT is performed, consisting of K successive IFFT operations of length L , each followed by a complex-real time-domain scaling that applies the prototype pulse, with an additional computational complexity of

$$\begin{aligned} C_{HT,KL} &= K(5L \log_2 L) + 2KL \quad [\text{FLOPs}] \\ &= N(5 \log_2 L + 2). \end{aligned} \quad (41)$$

In all, the total complexity of the ISFFT-HT based OTFS modulator/demodulator is then given by

$$\begin{aligned} C_{OTFS,KL} &= C_{ISFFT,KL} + C_{HT,KL} \\ &= 5N(\log_2 NL) + 2N. \quad [\text{FLOPs}] \end{aligned} \quad (42)$$

Alternatively, if pulse-shaping is performed directly in the delay-Doppler domain via 2D convolution in the prior, a single IDZT approach may be employed. The IDZT on a $K \times L$ delay-Doppler block is implemented using K IFFTs of length L with some sample interleaving operation, where the latter is approximated to have negligible computation complexity (only space complexity), such that the total complexity required for the IDZT is

$$C_{Zak} = K(5L \log_2 L) = 5N \log_2 L. \quad [\text{FLOPs}] \quad (43)$$

The 2D convolution for the pulse shaping in the delay-Doppler grid of size $K \times L$, is efficiently implemented using an FFT-based approach instead of the inefficient naive convolution, which involves a forward 2D FFT, a point-wise multiplication with the pulse's 2D FFT, and an inverse 2D FFT back to the delay-Doppler, i.e.,

$$\mathbf{X}_{DD,ps} = \text{IDFT}_{2D} \left(\text{DFT}_{2D}(\mathbf{X}_{DD}) \odot \text{DFT}_{2D}(\mathbf{P}) \right), \quad (44)$$

where $\mathbf{X}_{DD} \in \mathbb{C}^{K \times L}$ is the delay-Doppler symbol block, $\mathbf{P} \in \mathbb{R}^{K \times L}$ is the real-valued pulse shaping filter in the delay-Doppler domain, and $\mathbf{X}_{DD,ps} \in \mathbb{C}^{K \times L}$ is the pulse-shaped delay-Doppler symbol block.

We may assume that the complexity of obtaining the FFT of the pulse filter, $DFT_{2D}(\mathbf{P})$, is negligible as it can be computed offline once, therefore the computational complexity is obtained for one FFT of size $K \times L$, one IFFT of size $K \times L$, and the element-wise multiplication of two matrices of size $K \times L$, yielding a total complexity of

$$C_{DDPs,KL} = 2 \cdot (5KL \log_2 KL) + 6KL \text{ [FLOPs]} \quad (45)$$

$$= 10N \log_2 N + 6N.$$

Therefore, in all, the total complexity of the Zak-OTFS modulator/demodulator with delay-Doppler pulse shaping is approximated as

$$C_{\text{Zak-OTFS}} = C_{\text{Zak}} + C_{DDPs,KL} \text{ [FLOPs]} \quad (46)$$

$$= 5N \log_2 L + 10N \log_2 N + 6N$$

$$= 5N \log_2 LN^2 + 6N$$

Comparing the modulator complexities including the pulse-shaping overheads of OFDM, AFDM, and the two OTFS implementations in (42) and (46), which are summarized in Table 1, it is evident that both OTFS approaches introduce significantly higher computational burdens compared to the OFDM due to their multi-stage transform structures and 2D processing requirements under practical systems³, while AFDM maintains a modest overhead over OFDM and therefore stands out as a more computationally efficient alternative.

TABLE 1: Computational complexity of key operations and total modulator/demodulator complexities in FLOPs, with $N = KL$.

Operation	Complexity (FLOPs)
$IDFT_N$	$5N \log_2 N$
$IDAFT_N$	$5N \log_2 N$
$ISFFT_{K,L}$	$5N \log_2 N$
$HT_{K,L}$	$5N \log_2 L + 2N$
$IDZT_{K,L}$	$5N \log_2 L$
1D pulse shaping	$12N$
DD pulse shaping	$10N \log_2 N + 6N$

Pulse-shaped Waveform	Complexity (FLOPs)
OFDM	$5N \log_2 N + 2N$
AFDM	$5N \log_2 N + 12N$
OTFS	$5N \log_2 N + 5N \log_2 L + 2N$
Zak-OTFS	$10N \log_2 N + 5N \log_2 L + 6N$

³Regarding FFT dimension flexibility, OFDM and AFDM support arbitrary FFT/IFFT sizes N with one-dimensional frequency-domain processing, enabling flexible numerology and resource allocation. In contrast, OTFS imposes strict integer divisibility constraints on the delay-Doppler grid dimensions $K, L \in \mathbb{N}$ such that $N = KL$, limiting design flexibility and potentially resulting in awkward FFT sizes for practical implementations and efficient computations.

Furthermore, in addition to the time complexity of arithmetic operations, in practical modem implementations, memory movement and on-chip buffering often dominate both latency and energy consumption, especially in high-throughput communication systems. In this perspective, the AFDM waveform requires only local element-wise multiplications for its additional processing, which do not necessitate global data reshaping beyond the existing FFT/IFFT buffering inherent in the system. Conversely, OTFS implementations may involve more complex data handling due to frequent reshaping operations under practical, non-ideal conditions, such as interleaving and reshaping required in the ISFFT and pulse shaping stages.

Given the above, beyond per-block computational complexity, it is essential to consider the scalability of AFDM and OTFS with respect to the number of subcarriers and antennas, especially for practical systems employing MIMO configurations at high bandwidths and data rates. Since the computational complexity and memory requirements of both AFDM and OTFS scale linearly with the number of antennas in MIMO systems, the relative overheads identified above remain consistent regardless of the antenna count, making the previous analysis directly applicable to MIMO scenarios as well, and thus promotes the scalability of AFDM in massive MIMO deployments for 6G and beyond.

B. Pilot Scheme and Channel Estimation

In this section, we discuss channel estimation strategies for AFDM in doubly dispersive channels, focusing on pilot design and estimation algorithms. Given the structural similarities between AFDM and OFDM, many established pilot schemes can be adapted to AFDM, albeit with modifications to account for the unique characteristics of the affine-frequency domain.

1) Pilot Schemes

Due to the structure of the effective channel matrix Ξ^{AFDM} as described in Section B, the usual pilot schemes for AFDM involve one or multiple pilot subcarriers [29], [79], each of which is isolated from other subcarriers by guard bands (in the DAFT domain) to capture the contribution of each path without interference properly.

In the case of the conventional single-pilot scheme [29], the transmitted symbol vector $\mathbf{x} \in \mathbb{C}^{N \times 1}$ in the affine-frequency domain is designed as

$$\mathbf{x} = [x_0, \dots, x_{m-Q}, \quad (47)$$

$$\underbrace{0, \dots, 0}_{Q}, x_m^{(\text{pil})}, \underbrace{0, \dots, 0}_{Q}, x_{m+Q}, \dots, x_{N-1}]^T,$$

where $x_m^{(\text{pil})}$ is the pilot at position m in the vector, surrounded by Q null subcarriers that serve as a guard band, and the remaining subcarriers are used to transmit data symbols, as shown in Fig. 5.

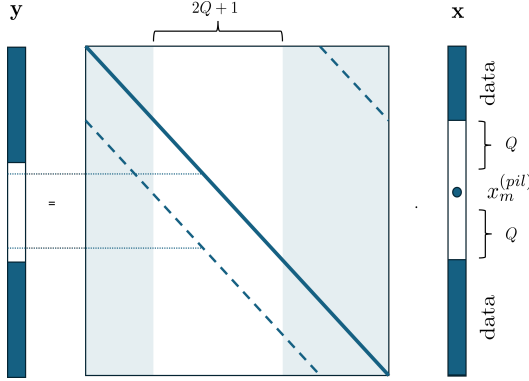


FIGURE 5: Transmitted pilot vector multiplexed with data \mathbf{x} (as in 47) in the affine-frequency domain and received signal \mathbf{y} .

Note that to avoid interference from the data subcarriers, the guard band width Q must satisfy [29], [79]

$$Q \geq (\ell_{\max} + 1)(2f_{\max} + 1) - 1, \quad (48)$$

where ℓ_{\max} and f_{\max} are the maximum normalized delay and maximum normalized digital Doppler shift of the doubly dispersive channel, respectively.

In the case of a multiple-pilot aided scheme, the pilot subcarriers must be separated by a distance of at least Q , which can improve the channel estimation performance (through the diversity of pilots), at the expense of a loss of spectral efficiency (SE), since each additional pilot involves at least $Q + 1$ subcarriers not used for data transmission.

To circumvent the SE loss, a guard interval-free pilot scheme has been proposed in [80], where the $2Q$ null subcarriers in (47) are substituted by data. Alternatively, a superimposed pilot scheme is also described in [81], theoretically optimizing the SE. In this case, pilot subcarriers $x_m^{(\text{pil})}$ are superimposed to the data x_m (i.e. $x_m + x_m^{(\text{pil})}$), with a distance Q between the added pilots. However, in both cases, channel estimation and data detection require specific processing at the receiver side, as discussed in the following.

In the case of a negligible Doppler shift or if all paths share a common Doppler shift and integer delays (which is a usual assumption in OFDM systems), then it becomes possible to separately estimate the channel frequency response and the Doppler shift in the frequency and time domains, respectively [82], while the estimation in the DAFT domain remains practicable. To this end, a single pilot aided scheme as in (47) can be considered without data multiplexing, i.e. \mathbf{x} consists of $N - 1$ null subcarriers with only one pilot $x_m^{(\text{pil})}$ at the m -th position.

In the frequency domain, the pilot vector is given by $\mathbf{x}_f = \mathbf{F} \cdot \mathbf{A}^H \cdot \mathbf{x}$, which is not tractable in general. However, according to [82], [83], \mathbf{x}_f has a simple and tractable expression in the special case of $q = 2N\lambda_1 \in \mathbb{Z}$, where the non-zero elements of \mathbf{x}_f are then constant modulus and equi-spaced with a distance $|q|$ between two consecutive pilot subcarriers in the frequency domain, starting with subcarrier $m_q = (m)_{|q|}$. Interestingly, setting $|q| \in \{2, 4\}$, the pilot

scheme is very similar to the pilot distribution described for the 5G signals [84], so that the estimation processing used for 5G signals can be used in AFDM. Furthermore, to limit the SE loss, it is also possible to multiplex pilot and data in the frequency domain or in the DAFT domain as in (47).

2) Channel Estimation in the DAFT Domain

In this section, we present the basics of channel estimation in the DAFT domain based on the pilot scheme described in (47). Other methods will be briefly discussed afterwards.

a: Integer Delay and Doppler

The estimation of the channel necessitates the estimation of $3P$ unknown parameters corresponding to the delay ℓ_p , the Doppler shift f_p , and the complex gain h_p for each of the paths $p = \{1, \dots, P\}$. As raised by the authors in [29], the common maximum likelihood (ML) estimation of the $3P$ parameters is intractable in practice. However, it is possible to estimate the parameters separately, as described below. First, it must be noticed that by substituting (47) into (34), we find that the elements y_k of \mathbf{y} , for $k \in \{(m - (Q - f_{\max}))_N, (m + f_{\max})_N\}$ are given by [54]

$$y_k = \begin{cases} [\Xi^{\text{AFDM}}]_{k,m} \cdot x_m^{(\text{pil})} + [\mathbf{Aw}]_k & \text{if } k = (m + N - \text{loc}_p)_N, \\ [\mathbf{Aw}]_k & \text{otherwise,} \end{cases} \quad (49)$$

where $\text{loc}_p = (f_p + \ell_p(2f_{\max} + 1))_N$.

This is illustrated in Fig. 5. Then, for any $\ell = \{0, 1, \dots, \ell_{\max}\}$, the ML estimation of f_ℓ is given by

$$\hat{f}_\ell = \arg \max_{k' \in \Omega_{k'}} |y_{k'}|^2, \quad (50)$$

where $\Omega_{k'} = [-f_{\max}, f_{\max}]$ and $k = (\ell \cdot 2f_{\max} + k')_N$.

If the number of paths P is known *a priori*, it corresponds to the P highest values of $|y_k|^2$ among the ℓ_{\max} calculated in (50). If P is unknown, it is suggested in [79] to set a threshold ζ depending on the SNR and to keep the P path whose value $|y_k|^2$ exceeds ζ .

Once (f_p, ℓ_p) , for $p = \{1, \dots, P\}$ is estimated, the estimate of the complex gains h_p can be obtained through

$$\hat{h}_p = \frac{[\Xi^{\text{AFDM}'}]_{k_p, m}^* \cdot y_{k_p}}{x_m^{(\text{pil})}} \quad (51)$$

where $k_p = (\ell_p \cdot 2f_{\max} + f_p)_N$, and the value $[\Xi^{\text{AFDM}'}]_{k_p, m}$ is generated using the estimates $(\hat{f}_p, \hat{\ell}_p)$.

b: Integer Delay and Fractional Doppler

In this part, we denote the integer and fractional parts of f_p by $f_p^{(i)} = \lfloor f_p \rfloor$ and $f_p^{(f)} = f_p - f_p^{(i)}$, respectively. As introduced in [29], the estimation of the $3P$ channel parameters in the case of fractional Doppler starts by the estimation of the integer part $f_p^{(i)}$ as in (49)-(50). Then, the fractional part $f_p^{(f)}$ is estimated through

$$\hat{f}_p^{(f)} = \arg \max_{f_p^{(f)} \in [-\frac{1}{2}, \frac{1}{2}]} \frac{\sum_{k' \in \Omega_{k'}} |[\Xi^{\text{AFDM}'}]_{k, m}^* y_{k'}|^2}{\sum_{k' \in \Omega_{k'}} |[\Xi^{\text{AFDM}'}]_{k, m}|^2}, \quad (52)$$

where $k = (\ell_p \cdot 2f_{\max} + k')_N$, and the value $[\Xi^{\text{AFDM}'}]_{k_p, m}$ is generated using the estimates $(\hat{f}_p = \hat{f}_p^{(i)} + f_p^{(f)}, \hat{\ell}_p)$.

Moreover, in practice, (52) is performed using a search on a fine discretization of $[-\frac{1}{2}, \frac{1}{2}]$, such that ultimately, the estimate of the complex gains h_p can be obtained through

$$\hat{h}_p = \frac{\sum_{k' \in \Omega_{k'}} [\Xi^{\text{AFDM}'}]_{k, m} y_k}{x_m^{(\text{pil})}}, \quad (53)$$

where the value $[\Xi^{\text{AFDM}'}]_{k_p, m}$ is generated using the estimates $(\hat{f}_p = \hat{f}_p^{(i)} + \hat{f}_p^{(f)}, \hat{\ell}_p)$.

c: Fractional Delay and Doppler

Finally, the problem of estimating both fractional delay and Doppler parameters can be particularly difficult or even untractable if $\mathbf{G}(\ell_p)$ is dense and Toeplitz as suggested in (16). However, according to the finite interpolation kernel, $\mathbf{G}(\ell_p)$ (and as illustrated in Figure 2) is a banded matrix with a relatively tight band diagonal of defined width $2B + 1$.

Furthermore, the matrix $\mathbf{G}(\ell_p)$ can be approximated to be circulant instead of Toeplitz, which becomes exact if a cyclic suffix is also used in addition to the CPP, or if a negative delay is applied previous to the demodulation process. In light of the above, by denoting $[g_{-B}, \dots, g_0, \dots, g_B]$ as the non-zero coefficients of the band diagonal of $\mathbf{G}(\ell_p)$, where $g_q = g(q - \ell_p)$, $p = -B, \dots, B$, $\mathbf{G}(\ell_p)$ can be rewritten as

$$\mathbf{G}(\ell_p) = \sum_{q=-B}^B g_q \cdot \mathbf{\Pi}^{\ell_p+q}. \quad (54)$$

Then, the discrete input-output relation is expressed as

$$\mathbf{r} = \left(\sum_{p=1}^P \sum_{q=-B}^B h_p \cdot \Phi_p \cdot \mathbf{V}^{f_p} \cdot g_q \cdot \mathbf{\Pi}^{\ell_p+q} \right) \cdot \mathbf{s} + \mathbf{w}. \quad (55)$$

Ordering the $P(2B + 1)$ tuples (p, q) as $\{(p=1, q=-B), \dots, (p=1, q=B), (p=2, q=-B), \dots, (p=P, q=B)\}$, and defining $u = \{1, \dots, P(2B + 1)\}$ as the corresponding indices, (55) can be rewritten in a final compact form as

$$\mathbf{r} = \left(\sum_{u=1}^{P(2B+1)} h'_u \cdot \Phi_u \cdot \mathbf{V}^{f_u} \cdot \mathbf{\Pi}^{\ell'_u} \right) \cdot \mathbf{s} + \mathbf{w}, \quad (56)$$

where $h'_u = h_p \cdot g_q$ and $\ell'_u = \ell_p + q$ are defined to highlight the similarity of (56) to the conventional IDID doubly dispersive channel model of (10).

Under this reformulation, it follows that the channel estimation methods that have been previously described for the IDID doubly dispersive channel, can be adapted to the fractional delay and Doppler case, under the new virtual path parameters $\{h'_u, \ell'_u, f_u\}$ for $u = \{1, \dots, P(2B + 1)\}$ and the deterministic structure now available through (15). This shows that AFDM allows accurate estimation of the Doppler shift and delay beyond the Nyquist rate, even though the signal is sampled at the Nyquist rate.

3) Special Case: OFDM-like Estimation Under Low Doppler
The previous sections presented the channel estimation explicitly in the DAFT domain native to the AFDM, considering fully doubly dispersive channels. However, in condition of low Doppler shift, the latter can be omitted, leading to $\mathbf{V}^{f_p} \approx \mathbf{I}_N$, and then Ξ^{OFDM} is diagonal with elements $(\Xi^{\text{OFDM}})_{n,n} = \sum_{p=1}^P h_p e^{-2j\pi \frac{\ell_p n}{N}}$.

Note that such conditions are the very channels usually assumed in OFDM systems, and therefore previous estimation methods for OFDM remain valid and are especially relevant if only the delay estimation is necessary. Indeed, it has been shown in [82] that channel estimation can also be performed in the frequency domain using the special cases of AFDM parameters described in [83].

In fact, suppose that $2N\lambda_1 \in \mathbb{Z}$ and $\frac{1}{2\lambda_1} \in \mathbb{Z}$, and that the pilot \mathbf{x} in (47) is now expressed as $\mathbf{x} = [0, \dots, 0, x_m^{(\text{pil})}, 0, \dots, 0]^T$. Then, the DFT of the AFDM transmit signal \mathbf{s} in (30), given by

$$\mathbf{z} = \mathbf{F}_N \cdot \mathbf{s} = \mathbf{F}_N \cdot \mathbf{A}^H \cdot \mathbf{x} \in \mathbb{C}^{N \times 1}, \quad (57)$$

has the following regular structure, for $k = \{0, 1, \dots, N-1\}$,

$$z_k = \begin{cases} \zeta_k \mathbb{1}_{(m-k) \bmod 2N\lambda_1 = 0}, & \text{if } \frac{1}{2\lambda_1} \text{ is even} \\ \zeta_k \mathbb{1}_{\frac{(m-k)}{N\lambda_1} \in \mathbb{Z} \setminus 2\mathbb{Z}}, & \text{if } \frac{1}{2\lambda_1} \text{ is odd} \end{cases}, \quad (58)$$

where $\mathbb{1}_\Omega$ is the indicator function of the elements belonging to the set Ω , and $\mathbb{Z} \setminus 2\mathbb{Z}$ is the subset of \mathbb{Z} corresponding to the odd integers.

Moreover, $\zeta_k \in \mathbb{C}$ is a constant modulus value (*i.e.* $|\zeta_k| = \zeta \in \mathbb{R}$ for any k) whose expression is detailed in [82], with the regular structure of \mathbf{z} illustrated in Fig. 6. It must be noticed that such equispaced pilots in the frequency domain are used in most of the communications standards based on OFDM, in particular, 4G/5G, and WiFi.

Based on this pilot structure leveraging on special cases of AFDM parameters, the AFDM demodulation in (34) can be now performed using a DFT matrix \mathbf{F}_N instead of \mathbf{A} ,

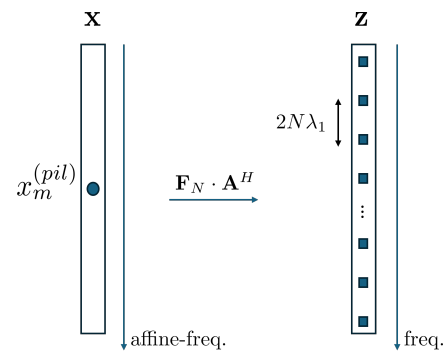


FIGURE 6: Regular structure of $\mathbf{z} = \mathbf{F}_N \cdot \mathbf{A}^H \cdot \mathbf{x}$ where $\mathbf{x} = [0, \dots, 0, x_m^{(\text{pil})}, 0, \dots, 0]^T$, in the special cases $2N\lambda_1 \in \mathbb{Z}$ and $\frac{1}{2\lambda_1} \in \mathbb{Z}$.

which yield

$$\begin{aligned}
 \mathbf{y}_f &= \mathbf{F}_N \cdot \mathbf{r} \\
 &= \mathbf{F}_N \left(\underbrace{\sum_{p=1}^P h_p \cdot \Phi_p \cdot \mathbf{V}^{f_p} \cdot \mathbf{G}(\ell_p)}_{\triangleq \Xi^{\text{OFDM}} \in \mathbb{C}^{N \times N}} \right) \mathbf{F}_N^H \cdot \mathbf{F}_N \mathbf{A}^H \cdot \mathbf{x} + \mathbf{F}_N \mathbf{w} \\
 &= \Xi^{\text{OFDM}} \mathbf{z} + \mathbf{F}_N \mathbf{w} \in \mathbb{C}^{N \times 1},
 \end{aligned} \tag{59}$$

where we recognize Ξ^{OFDM} because $2N\lambda_1 \in \mathbb{Z}$, and in turn $\Phi_p = \mathbf{I}_N$.

Furthermore, the subscript f indicates the received AFDM pilot signal in the frequency domain. In this special case, the usual frequency domain channel estimation used in OFDM [13], [14], [85], [86] can be performed based on (59). In addition, it is worth noting that data can be multiplexed across pilot subcarriers, making AFDM fully backward-compatible with OFDM. Otherwise, in doubly dispersive channels, data can be multiplexed in the affine-frequency domain as previously described in (47) and Fig. 5. Thus, AFDM is very flexible, as the modulation/demodulation and channel estimation domains and methods can be adapted to the channel severity using a unique pilot scheme.

C. Signal Detection and Receiver Architectures

Following the acquisition of channel state information (CSI) via the estimation schemes detailed in the previous section, the receiver must recover the data vector \mathbf{x} from the received affine-frequency domain signal \mathbf{y} . The structural insights provided by the generalized FDFD model are also significant in this context, as by reformulating the complex fractional-delay channel into the structured virtual IDID representation as defined in (56), the receiver can leverage established detection algorithms with well-defined interference cancellation targets. In this, depending on the interplay between the detector and decoder, AFDM receivers are categorized into two primary architectures, as illustrated in Fig. 7.

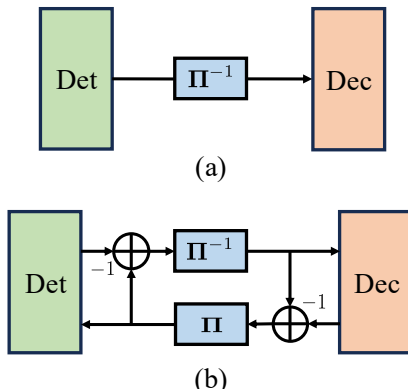


FIGURE 7: Illustration of the AFDM receivers using (a) non-outer iterations and (b) turbo iterations between detectors and decoders.

The first category consists of one-shot receivers that perform detection without outer iterations for improved computational efficiency. In contrast, the second category comprises turbo receivers designed for coded AFDM systems, which iteratively exchange extrinsic log-likelihood ratios (LLRs) between the detector and the decoder to approach the channel capacity. We first examine AFDM receiver architectures that operate without outer iterations, then discuss turbo receivers.

1) One-shot Receivers (No outer iterations)

From an algorithmic perspective, the detection algorithms of AFDM receivers can be broadly categorized into two groups: linear detectors and sparse channel-enabled detectors.

a) Linear detectors: This group comprises linear detectors, such as zero-forcing (ZF) and linear minimum mean-square error (LMMSE) receivers [44], [87]–[90]. Based on the input-output relationship of AFDM in (34), the ZF and minimum mean-square error (MMSE) detectors can be respectively formulated as

$$\hat{\mathbf{x}}^{\text{ZF}} = [(\Xi^{\text{AFDM}})^H \Xi^{\text{AFDM}}]^{-1} (\Xi^{\text{AFDM}})^H \mathbf{y}, \tag{60}$$

$$\hat{\mathbf{x}}^{\text{MMSE}} = [(\Xi^{\text{AFDM}})^H \Xi^{\text{AFDM}} + \sigma_w^2 \mathbf{I}_N]^{-1} (\Xi^{\text{AFDM}})^H \mathbf{y}. \tag{61}$$

The complexity of calculating the MMSE detector directly is on the order of $\mathcal{O}(N^3)$, which is excessive for large-scale AFDM systems. Upon exploiting matrix factorization techniques, such as LU factorization [91], Cholesky decomposition [92], and LDL factorization [93], [94], the complexity of linear detectors can be mitigated. As an example, the LDL factorization-based MMSE detector is elaborated in this section to provide further insight.

LDL factorization-based MMSE detector: Owing to the sparsity pattern of the effective DAFT-domain channel, the matrix Γ is Hermitian positive-definite with the lower and upper bandwidth J . By exploiting the banded structure enables the use of an LDL factorization and the trimming matrix $\mathbf{T} = [\mathbf{I}_N]_{Q-(\alpha_{\max}+k_v):N-(\alpha_{\max}+k_v)-1,:}$, where Γ is decomposed into a unit lower-triangular matrix \mathbf{L} containing only J sub-diagonals and a diagonal matrix \mathbf{D} . This decomposition reduces both memory usage and computational complexity to $\mathcal{O}(J^2N)$, representing a substantial improvement over conventional MMSE inversion.

Once the LDL factors are obtained, the equalization step reduces to solving two triangular systems and one diagonal system, all of which can be efficiently implemented. The complete LDL-based low-complexity MMSE equalization procedure is summarized in **Algorithm 1**.

b) Sparse channel-enabled detectors: The second group consists of sparse channel-enabled detectors that exploit the inherent sparsity of the effective DAFT-domain channel matrix in (34). These detectors typically adopt low-complexity iterative schemes, including maximal ratio combining (MRC) [29], message passing (MP) [33], [95]–[98], and expectation propagation (EP) algorithms [99].

Algorithm 1 LDL factorization-based MMSE detector

- 1: Construct $\Xi^{\text{AFDM}} = \Xi^{\text{AFDM}} \mathbf{T}^H$.
- 2: Form the banded matrix $\Gamma = (\Xi^{\text{AFDM}})^H \Xi^{\text{AFDM}} + \sigma_w^2 \mathbf{I}_N$.
- 3: Compute the LDL factorization $\Gamma = \mathbf{L} \mathbf{D} \mathbf{L}^H$, where \mathbf{L} is a lower triangular matrix with J sub-diagonals and \mathbf{D} is diagonal.
- 4: Solve the lower triangular system $\mathbf{L} \mathbf{f} = \mathbf{y}$.
- 5: Solve the diagonal system $\mathbf{D} \mathbf{g} = \mathbf{f}$.
- 6: Solve the upper triangular system $\mathbf{L}^H \mathbf{d} = \mathbf{g}$.
- 7: Compute the MMSE estimate $\tilde{\mathbf{x}} = (\Xi^{\text{AFDM}})^H \mathbf{d}$.

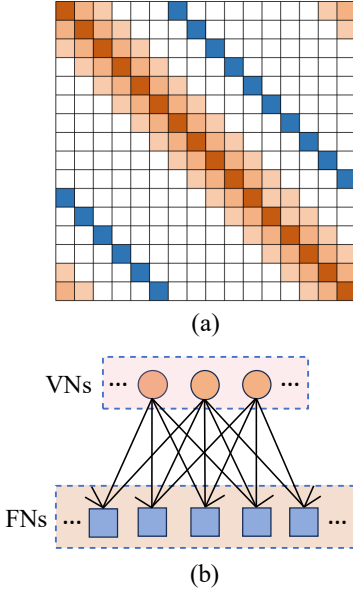


FIGURE 8: Illustration of (a) the effective DAFT-domain channel matrix with two paths and (b) the corresponding factor graph.

Fig. 8 illustrates an example of the effective channel matrix and its associated factor-graph representation, where each variable node (VN) corresponds to a transmitted symbol and each factor node (FN) represents a received symbol connected to a subset of VNs determined by the channel structure. During message passing, probabilistic information is iteratively exchanged between VNs and FNAs to refine the symbol estimates progressively. Next, we provide more details on the MRC and MP detectors, as the main examples.

MRC detector: During the t -th iteration, each symbol $\tilde{x}^{(t)}[n]$ is sequentially updated according to

$$\tilde{x}^{(t)}[n] = \frac{g_n^{(t)}}{d_n + \sigma_w^2}, \quad (62)$$

where

$$g_n^{(t)} = \sum_{l \in \mathcal{L}_n} [\Xi^{\text{AFDM}}]_{l,n}^* \Delta^{(t-1)}[l] + d_n \tilde{x}^{(t-1)}[n], \quad (63)$$

$$d_n = \sum_{l \in \mathcal{L}_n} |[\Xi^{\text{AFDM}}]_{l,n}|^2, \quad (64)$$

with $\Delta^{(t-1)}$ denoting the residual vector at the $(t-1)$ -th iteration and $\Delta^{(t-1)}[l]$ as its l -th element, and \mathcal{L}_n represents

the set of non-zero row indices in the n -th column of the truncated effective channel Ξ^{AFDM} .

After each symbol update, the corresponding residual entries are refined via

$$\Delta^{(t)}[l] = \Delta^{(t-1)}[l] - [\Xi^{\text{AFDM}}]_{l,n} (\tilde{x}^{(t)}[n] - \tilde{x}^{(t-1)}[n]), \quad (65)$$

for all $l \in \mathcal{L}_n$. Once all symbols have been updated, the refined estimates are used for interference cancellation in the subsequent iteration. This iterative procedure continues until the change between two consecutive symbol vectors becomes negligible or the maximum number of iterations T is reached. This iteration within a single iterative algorithm is not to be confused with turbo iterations between the detector and decoder, which will be discussed later.

MP detector: From onwards, we assume that the indices ℓ_p and f_p are integer-valued for general $p = \{1, \dots, P\}$, either for IDID scenarios (10) or following the generalized FDFD model of (56). First, the AFDM input-output relation is rewritten in scalar form as

$$y[a] = \sum_{p=1}^P h_p \cdot e^{j \frac{2\pi}{N} (N c_1 \ell_p^2 - b \ell_p + N c_2 (b^2 - a^2))} \cdot x[b] + \tilde{w}[a], \quad (66)$$

for $a = \{1, \dots, N\}$. From the vectorized AFDM model in (34), the received vector $\mathbf{y} \in \mathbb{C}^N$ and noise vector $\tilde{\mathbf{w}} \in \mathbb{C}^N$ contain elements $y[a]$ and $\tilde{w}[a]$, respectively. According to (66), the non-zero entries of the effective matrix Ξ^{AFDM} exhibit a structured sparsity pattern: the a -th row contains non-zero elements at indices $(a + \text{loc}_p)_N$, while the non-zero entries of the b -th column appear at indices $(b - \text{loc}_p)_N$.

Then, by letting I_a as the set of non-zero column indices in row a , and D_b as the set of non-zero row indices in column b , the system model (34) naturally corresponds to a sparse factor graph with N VNs representing \mathbf{x} and N FNAs representing \mathbf{y} . Each observation node $y[a]$ connects to P variable nodes $\{x[b] : b \in I_a\}$, while each variable node $x[b]$ connects to P observation nodes $\{y[a] : a \in D_b\}$.

Directly from (34), the optimal joint maximum a posteriori (MAP) detector is given by

$$\hat{\mathbf{x}} = \arg \max_{\mathbf{x} \in \mathcal{X}^N} \Pr(\mathbf{x} \mid \mathbf{y}, \Xi^{\text{AFDM}}), \quad (67)$$

but this approach requires exponential complexity in N . To avoid this, a symbol-wise MAP approximation is adopted as

$$\begin{aligned} \tilde{x}[b] &= \arg \max_{a_j \in \mathcal{X}} \Pr(x[b] = a_j \mid \mathbf{y}, \Xi^{\text{AFDM}}) \\ &= \arg \max_{a_j \in \mathcal{X}} \frac{1}{M} \Pr(\mathbf{y} \mid x[b] = a_j, \Xi^{\text{AFDM}}) \end{aligned} \quad (68a)$$

$$\approx \arg \max_{a_j \in \mathcal{X}} \prod_{a \in D_b} \Pr(y[a] \mid x[b] = a_j, \Xi^{\text{AFDM}}), \quad (68b)$$

where (68a) assumes equiprobable symbols, (68b) uses an independence approximation motivated by the sparsity of Ξ^{AFDM} , and the interference terms $\zeta_{b,a}^{(t)}$ defined in (69) are assumed independent for fixed b .

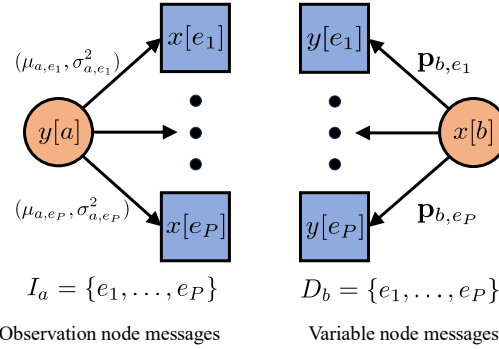


FIGURE 9: The factor graph structure of the MP algorithm.

To address the intractability of the full (68b), an MP detector is employed whose complexity only scales linearly with N . For each observation $y[a]$, the contribution of $x[b]$ is isolated, and the sum of remaining interference terms is approximated as a Gaussian random variable with mean and variance computed in closed form, whose factor is shown in Fig. 9. In the MP framework, observation-to-variable messages consist of these Gaussian parameters, whereas variable-to-observation messages consist of probability mass functions (PMFs) over the constellation alphabet, $\mathbf{p}_{b,a}^{(t)} = \{p_{b,a}^{(t)}(a_j) : a_j \in \mathcal{X}\}$.

Given above, the t -th iteration of the MP algorithm proceeds as follows. First, the interference term $\zeta_{b,a}^{(t)}$ are defined as

$$\zeta_{a,b}^{(t)} = \sum_{e \in D_b, e \neq b} x[e] \cdot [\Xi^{\text{AFDM}}]_{a,e} + \tilde{w}[a]. \quad (69)$$

Next, the mean $\mu_{a,b}^{(t)}$ and variance $(\sigma_{a,b}^{(t)})^2$ are given by

$$\mu_{a,b}^{(t)} = \sum_{e \in I_a, e \neq b} \sum_{j=1}^M p_{e,a}^{(t-1)}(a_j) \cdot a_j \cdot [\Xi^{\text{AFDM}}]_{a,e}, \quad (70)$$

$$\begin{aligned} (\sigma_{a,b}^{(t)})^2 = & \sum_{e \in I_a, e \neq b} \left(\sum_{j=1}^M p_{e,a}^{(t-1)}(a_j) \cdot |a_j|^2 \cdot \left| [\Xi^{\text{AFDM}}]_{a,e} \right|^2 \right. \\ & \left. - \left| \sum_{j=1}^M p_{e,a}^{(t-1)}(a_j) \cdot a_j \cdot [\Xi^{\text{AFDM}}]_{a,e} \right|^2 \right) + \sigma_w^2. \end{aligned} \quad (71)$$

From (66), the corresponding channel coefficient is

$$[\Xi^{\text{AFDM}}]_{a,e} = h_p \cdot e^{j \frac{2\pi}{N} (N c_1 \ell_p^2 - q \ell_p + N c_2 (q^2 - a^2))}, \quad (72)$$

where $q = (a + \text{loc}_p)_N$. The, the updated PMFs are computed as

$$p_{b,a}^{(t)}(a_j) = \Delta \tilde{p}_{b,a}^{(t)}(a_j) + (1 - \Delta) p_{b,a}^{(t-1)}(a_j), \quad (73)$$

where $\Delta \in (0, 1]$ is a damping factor, and

$$\tilde{p}_{b,a}^{(t)}(a_j) \propto \prod_{e \in D_b, e \neq a} \Pr(y[e] | x[b] = a_j, \Xi^{\text{AFDM}}) \quad (74)$$

$$= \prod_{e \in D_b, e \neq a} \frac{\xi^{(t)}(e, b, j)}{\sum_{m=1}^M \xi^{(t)}(e, b, m)}, \quad (75)$$

Algorithm 2 MP-based detector

Input: Receive signal \mathbf{y} and channel matrix Ξ^{AFDM} .
Preparation: $\mathbf{p}_{b,a}^{(0)} = 1/M, b = 0, \dots, N-1, a \in D(b)$.
for $t = 1$ to T_{max} **do**
 3: Observation nodes $y[a]$ compute means $\mu_{a,b}^{(t)}$ and variances $(\sigma_{a,b}^{(t)})^2$ via (70) and (71) based on $\mathbf{p}_{b,a}^{(t-1)}$, and pass them to $\{x[b] : b \in I_a\}$.
 4: Variable nodes $x[b]$ update $\mathbf{p}_{b,a}^{(t-1)}$ via (73), and pass them to $\{y[a] : a \in D_b\}$.
 5: Calculate convergence indicator $\eta^{(t)}$.
 6: Update the decision on the transmitted symbols $x[c]$ for $c = 1, \dots, N$, if needed.
 7: **if** Stopping criteria are satisfied
 8: **break**
 9: **end for**
 10: **return** $\hat{\mathbf{x}}$.

with

$$\xi^{(t)}(e, b, m) = \exp \left(- \frac{\left| y[e] - \mu_{e,b}^{(t)} - a_m \cdot [\Xi^{\text{AFDM}}]_{a,e} \right|^2}{(\sigma_{e,b}^{(t)})^2} \right), \quad (76)$$

where the channel coefficient $[\Xi^{\text{AFDM}}]_{e,b}$ is

$$[\Xi^{\text{AFDM}}]_{e,b} = h_p \cdot e^{j \frac{2\pi}{N} (N c_1 \ell_p^2 - b \ell_p + N c_2 (b^2 - u^2))}, \quad (77)$$

with $u = (b - \text{loc}_p)_N$. Then, the symbol estimate is updated as $\hat{x}[b] = \arg \max_{a_j \in \mathcal{X}} p_b^{(t)}(a_j)$. Within the above steps, convergence is measured as

$$\eta^{(t)} = \frac{1}{N} \sum_{b=1}^N \mathbb{I} \left(\max_{a_j \in \mathcal{X}} p_b^{(t)}(a_j) \geq 1 - \gamma \right), \quad (78)$$

for a small threshold $\gamma > 0$, where

$$p_b^{(t)}(a_j) = \prod_{e \in D_b} \frac{\xi^{(t)}(e, b, j)}{\sum_{m=1}^M \xi^{(t)}(e, b, m)}. \quad (79)$$

Finally, the MP detector, as summarized in **Algorithm 2**, terminates when one of the following conditions is met at the end of each iteration: a) $\eta^{(t)} = 1$; b) $\eta^{(t)} < \eta^{(t^*)} - \epsilon$; c) $t = T_{\text{max}}$; where t^* is the iteration with the largest $\eta^{(t)}$ for $1 \leq t^* < t$;

2) Turbo Receiver

Alternative to the one-shot receivers where there are no outer iterations between the detector and the decoder, AFDM turbo receivers have been investigated in [88], [95], [100]. As shown in 7(b), a turbo receiver operates by iteratively exchanging soft reliability information between the detector and the channel decoder, enabling both modules to refine their estimates progressively.

Unlike conventional receivers that perform detection and decoding in isolation, which is depicted in 7(a), a turbo receiver leverages the fact that the channel decoder can provide highly informative soft outputs, which in turn help the equaliser to suppress residual interference more effectively.

Specifically, the extrinsic LLR output by the symbol-to-bit converter (SBC) after the detector can be formulated as [101]

$$L_e(c_{n,j}) \quad (80)$$

$$= \ln \frac{\sum_{\forall s_i: s_{i,j}=0} p(\hat{x}_n | \mathbf{c}_n = \mathbf{s}_i) \prod_{\forall j': j' \neq j} P(c_{n,j'} = s_{i,j'})}{\sum_{\forall s_i: s_{i,j}=1} p(\hat{x}_n | \mathbf{c}_n = \mathbf{s}_i) \prod_{\forall j': j' \neq j} P(c_{n,j'} = s_{i,j'})},$$

where \hat{x}_n denotes the n th estimated element, \mathbf{c}_n is the transmit bit sequence corresponding to x_n , \mathbf{s}_i represents the i th bit pattern associated with the constellation point $a_i \in \mathcal{X}$, and $s_{i,j}$ is the j th bit of \mathbf{s}_i .

This iterative feedback loop allows the system to approach optimal joint detection performance with substantially lower computational complexity. The primary advantage of a turbo receiver is its ability to exploit coding gain and diversity gain simultaneously. After each iteration, the improved extrinsic information helps mitigate ICI, reduce error propagation, and reshape the effective channel into a more favourable form for subsequent decoding. This makes turbo receivers particularly powerful in doubly selective or highly dispersive environments, where the detector alone is insufficient. Additionally, turbo processing is robust to imperfect channel conditions, delivers near-capacity performance in many scenarios, and is flexible enough to be applied to various modulation and coding schemes.

In summary, while the distinct matrix structure of AFDM necessitates specialized internal detection logic, such as LDL-based banded equalization or sparse factor-graph processing, the high-level architectural principles remain entirely consistent with legacy OFDM receivers. Therefore, the transition from OFDM receiver to AFDM receiver primarily involves replacing the core detection block, while the surrounding receiver infrastructure remains fundamentally unchanged. This compatibility ensures that the extensive ecosystem of receiver optimization techniques developed for 5G can be directly extended to AFDM, providing a low-risk, high-reward evolutionary path for 6G signal processing.

D. Extension to MIMO-AFDM Systems

1) Channel Estimation in MIMO-AFDM

The principle of MIMO-AFDM transmission and channel estimation has been investigated in [102]. It can be interpreted as an extension of SISO-AFDM systems in Section IV-B. In a $N_r \times N_t$ system, it is possible to discriminate the channels if the pilots are distributed for any transmit antenna as

$$\mathbf{x}_{n_t} = [..., \underbrace{0, \dots, 0}_Q, x_{m_{n_t}}^{(\text{pil})}, \underbrace{0, \dots, 0}_Q, \dots, ...]^T, \\ \mathbf{x}_{n_t+1} = [..., \dots, \underbrace{0, \dots, 0}_Q, x_{m_{n_t+1}}^{(\text{pil})}, \underbrace{0, \dots, 0}_Q, \dots]^T, \quad (81)$$

where \mathbf{x}_{n_t} is the $N \times 1$ vector transmitted at the n_t th antenna, and $m_{n_t} = (Q + 1)n_t - 1$.

At the n_r th receive antenna, the $N \times 1$ vector \mathbf{y}_{n_r} can be expressed as $\mathbf{y}_{n_r} = \mathbf{R}_{n_r} \bar{\mathbf{y}}$, where $\bar{\mathbf{y}}$ is defined in (36) and \mathbf{R}_{n_r} is the $N \times (N_r \cdot N)$ size matrix that extracts the components of $\bar{\mathbf{y}}$ from the $(n_r N)$ -th to the $(n_r + 1)N$ -th index.

Then \mathbf{y}_{n_r} can be derived from (36) as

$$\mathbf{y}_{n_r} = \left(\sum_{p=1}^P h_p \cdot \Theta_{p,n_r} \otimes \Xi_p^{\text{AFDM}} \right) \bar{\mathbf{x}} + \mathbf{w}_{n_r} \in \mathbb{C}^{N \times 1} \\ = \sum_{n_t=1}^{N_t} \left(\sum_{p=1}^P h_p \cdot (\Theta_{p,n_r})_{n_t} \Xi_p^{\text{AFDM}} \right) \mathbf{x}_{n_t} + \mathbf{w}_{n_r}, \quad (82)$$

where Θ_{p,n_r} corresponds to the n_r th row of the matrix Θ_p , and $\mathbf{w}_{n_r} = \mathbf{R}_{n_r} \tilde{\mathbf{w}}$.

From (81) and Fig. 5, it can be noticed that the N_t channels can be estimated using \mathbf{y}_{n_r} and the methods that have been previously described in the SISO case. In turn, the overall $N_r \cdot N_t$ channels can be estimated using $\bar{\mathbf{y}}$. Note that the MIMO channel estimation methods using the pilot distribution (81) [102] is very similar to the multiple pilot-aided channel estimation in the SISO system [79].

2) Special Cases of MIMO AFDM

Similarly to Section 3, we assume that the Doppler shift is small enough to be omitted, like in usual OFDM systems. Then, according to [103], it becomes possible to perform digital beamforming (precoding in DL or combining in UL) in the frequency domain. In fact, for any $n_t = \{1, \dots, N_t\}$ and $n_r = \{1, \dots, N_r\}$ we have

$$\mathbf{y}_{f,n_r} = \Xi_{n_r,n_t}^{\text{OFDM}} \mathbf{z}_{n_t} + \mathbf{w}_{f,n_r} \in \mathbb{C}^{N \times 1}, \quad (83)$$

where \mathbf{y}_{f,n_r} is the received AFDM symbol in the frequency domain on the n_r th antenna, $\mathbf{z}_{n_t} = \mathbf{F}_N \cdot \mathbf{A}^H \cdot \mathbf{x}_{n_t}$ is the transmitted AFDM symbol in the frequency domain on the n_t th antenna, $\mathbf{f} = \mathbf{F}_N \mathbf{w}_{n_r}$ is the AWGN, and $\Xi_{n_r,n_t}^{\text{OFDM}}$ is the diagonal channel matrix (due to low Doppler). Since the latter is diagonal, no inter-carrier interference occurs, so we can rewrite the MIMO input-output relation (83) for any subcarrier $k = \{1, \dots, N\}$ as

$$\mathbf{y}_{f,k} = \Xi_k^{\text{OFDM}} \mathbf{z}_k + \mathbf{w}_{f,k} \in \mathbb{C}^{N_r \times 1}, \quad (84)$$

where $\mathbf{z}_k \in \mathbb{C}^{N_t \times 1}$, and $\Xi_k^{\text{OFDM}} \in \mathbb{C}^{N_r \times N_t}$. Assuming that $n_t \geq n_r$, \mathbf{z}_k can be pre- or post-coded to perform digital beamforming similar to MIMO-OFDM systems. Thus, by denoting $\mathbf{U} \in \mathbb{C}^{N_t \times N_t}$ the precoding matrix, \mathbf{z}_k can be substituted by $\mathbf{U} \cdot \mathbf{z}_k$ in (84). Among the wide variety of digital beamforming methods, one can cite the usual zero forcing (ZF) method, which is given by:

$$\mathbf{U} = (\Xi_k^{\text{OFDM}})^H \cdot (\Xi_k^{\text{OFDM}} (\Xi_k^{\text{OFDM}})^H)^{-1}. \quad (85)$$

The main advantage of the ZF is the diagonalization of the channel, thereby leading to interference-free inter-user equipment (UE) transmission. However, the problem must be well-conditioned or the matrix $\Xi_k^{\text{OFDM}} (\Xi_k^{\text{OFDM}})^H$ may be not invertible. More generally, it is worth noting that in weak Doppler conditions, digital beamforming in AFDM is very similar to OFDM.

In addition to the previous observation, it is worth mentioning that in the special cases of AFDM parameter [83] where $2N\lambda_1 \in \mathbb{Z}$ and $\frac{1}{2\lambda_1} \in \mathbb{Z}$, subcarriers can be orthogonal in both the DAFT and the frequency domains. It is then possible to perform channel estimation in the frequency domain, as described in Section 3, along with frequency-domain beamforming.

E. Multiple Access and Coexistence with OFDM

The flexibility and backward compatibility of AFDM make it particularly suitable for supporting efficient, resilient multiple access in complex electromagnetic environments. Specifically, AFDM has a significant advantage: one can easily configure c_1 for different users based on their moving speeds to achieve robust transmissions. This is useful for supporting multiuser communications in, for example, 6G NTNs, in which both base stations (e.g., high-altitude platform stations and low-earth-orbit satellites) and user terminals (e.g., flying drones, connected vehicles, high-speed trains) may move at varying speeds. The waveform coexistence between AFDM and OFDM was studied in [104], revealing that each waveform admits a sparse, comb-like representation in the other's native domain. By exploiting the full diversity property of AFDM, a rate-splitting multiple access (RSMA) framework was reported in [105], in which the coexistence between AFDM and OFDM was investigated. A downlink AFDM-RSMA scheme was proposed in [106] with the key idea that private messages of different users are mapped onto orthogonal chirps, while common messages span all the chirps. To support massive connectivity over high mobility channels, the integration of AFDM and sparse code multiple access (SCMA), called AFDM-SCMA, was studied in [95]. As a promising code-domain non-orthogonal multiple access scheme [95], SCMA empowered by OFDM may not work well under carrier frequency offsets [107] or Doppler shifts. It was shown that AFDM-SCMA achieves excellent error-rate performance by leveraging the complementary strengths of these two wireless techniques.

In the sequel, we briefly introduce affine frequency division multiple access (AFDMA) and its coexistence with orthogonal frequency division multiple access (OFDMA), AFDMA per block or per subcarrier, and MIMO-AFDMA.

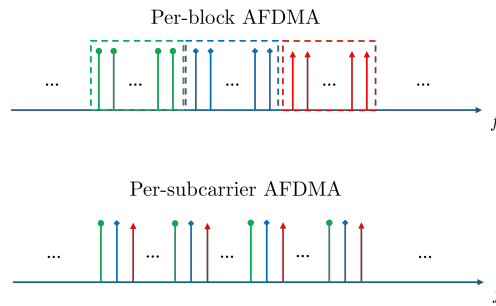


FIGURE 10: Frequency mapping strategies for AFDMA: per-block (top) and per-subcarrier (bottom) approaches.

1) General AFDMA and Coexistence with OFDMA

Two distinct paradigms may facilitate AFDMA, as illustrated in Fig. 10: *a*) per-block multiplexing and *b*) per-subcarrier multiplexing. These schemes enable multiple UEs to share the available bandwidth while maintaining compatibility with legacy OFDMA systems.

a: Per-Block AFDMA

In the per-block approach, K_{UE} users share a total bandwidth of N subcarriers, and each user $k_{\text{UE}} \in \{1, \dots, K_{\text{UE}}\}$ is allocated $N_{k_{\text{UE}}}$ subcarriers such that $N = \sum_{k_{\text{UE}}=1}^{K_{\text{UE}}} N_{k_{\text{UE}}}$. The composite transmit signal is expressed as

$$\mathbf{s} = \mathbf{F}_N^H \cdot \left[(\mathbf{F}_{N_1} \mathbf{s}_1)^T, \dots, (\mathbf{F}_{N_{K_{\text{UE}}}} \mathbf{s}_{K_{\text{UE}}})^T \right]^T, \quad (86)$$

where $\mathbf{s}_{k_{\text{UE}}} = \mathbf{A}_{k_{\text{UE}}}^H \mathbf{x}_{k_{\text{UE}}} \in \mathbb{C}^{N_{k_{\text{UE}}} \times 1}$ represents the chirped sub-signal of the k_{UE} -th user.

At the receiver, the composite signal is decomposed in the frequency domain via an N -point DFT \mathbf{F}_N , after which the individual user signals are recovered using UE-specific AFDM demodulation matrices. Given the above, a primary advantage of per-block AFDMA is its native support for coexistence between AFDM and OFDM. Since the sub-signals are orthogonal in the frequency domain, an AFDM sub-block can be replaced by an OFDM sub-block ($\mathbf{x}_{k_{\text{UE}}}$) without inducing inter-carrier interference, allowing for transparent spectral sharing between the two waveforms.

b: Per-Subcarrier AFDMA

As an alternative, per-subcarrier AFDMA leverages specific AFDM parameter configurations where $2N\lambda_1 \in \mathbb{Z}$ and $1/(2\lambda_1) \in \mathbb{Z}$, as discussed in Section 3. Under these conditions, a data element mapped to an affine-frequency index m is spread across specific frequency-domain indices k satisfying $(k)_{2N\lambda_1} = (m)_{2N\lambda_1}$. By allocating subcarriers with index $(m)_{2N\lambda_1} = r$ to a given user, up to $K_{\text{UE}} = 2N\lambda_1$ users can be multiplexed. The resulting transmit signal is given by

$$\mathbf{s} = \mathbf{A}^H \cdot \sum_{k_{\text{UE}}=0}^{2N\lambda_1-1} \mathbf{x}_{k_{\text{UE}}}, \quad (87)$$

where $\mathbf{x}_{k_{\text{UE}}}$ contains non-zero symbols only at indices $k_{\text{UE}} + n(2N\lambda_1)$.

Unlike the per-block approach, per-subcarrier AFDMA ensures subcarrier orthogonality in both the affine-frequency and frequency domains. This allows for fine-grained multiplexing of AFDM and OFDM symbols within the same block, as

$$\mathbf{s} = \mathbf{A}^H \cdot \sum_{k_{\text{UE}} \neq i}^{2N\lambda_1-1} \mathbf{x}_{k_{\text{UE}}} + \mathbf{F}^H \mathbf{x}_i, \quad (88)$$

where user i utilizes OFDM.

The resulting hybrid signal is easily separable at the receiver, facilitating flexible multi-user access under coexisting OFDM and AFDM signalling.

2) MIMO-AFDMA

Based on the established extension of AFDM to MIMO systems as discussed in the previous sections, and acknowledging the multi-user frameworks in legacy MIMO-OFDM, we also consider the adaptation of AFDM to multi-user MIMO scenarios, referred to as MIMO-AFDMA. MIMO-AFDMA further extends multi-user capabilities by enabling simultaneous communication between a base station and multiple UEs through spatial and domain-specific multiplexing, as illustrated in Fig. 11. We present a general overview of MIMO-AFDMA operation in both the downlink (DL) and uplink (UL).

In the DL, with $N_r \geq K_{UE}$, the first $(Q + 1)N_r$ indices of each transmit vector \mathbf{x}_{n_t} are reserved for pilot symbols to facilitate channel acquisition. The remaining indices are used for data, formatted as

$$\mathbf{x}_{n_t} = [0, \dots, 0, \underbrace{0, \dots, 0}_Q, \mathbf{x}_d^{(0)}, \dots, 0, \underbrace{\dots, 0, \dots, 0}_Q, \mathbf{x}_d^{(K_{UE}-1)}]^T, \quad (89)$$

where $\mathbf{x}_d^{(k_{UE})}$ represents the data payload for the k_{UE} -th user.

Each data block is isolated by guard bands of Q zero samples to prevent inter-user interference at the receiver. Since all transmit antennas broadcast the data blocks, users can exploit spatial diversity to improve detection reliability.

In the UL, the N available subcarriers are divided into subsets of contiguous subcarriers allocated to individual UEs based on throughput requirements. Each UE transmits its specific payload $\mathbf{x}_{k_{UE}}$, consisting of an embedded pilot and the data block $\mathbf{x}_d^{(k_{UE})}$. This domain partitioning ensures that multiple users can transmit asynchronously in high-mobility environments while minimizing mutual interference, thanks to AFDM's intrinsic Doppler robustness.

Interestingly, it is also possible to spatially multiplex AFDM and OFDM signals without interference, such as illustrated in Fig. 11 where $n_t = 4$ and two UEs are using OFDM. Mathematically, it corresponds to the multiplexing of AFDM and OFDM data within \mathbf{z}_k in (84). This shows the possible coexistence of AFDM and OFDM within the same communication system, and, once again, the backward compatibility of AFDM with OFDM, particularly in conditions of relatively low Doppler.

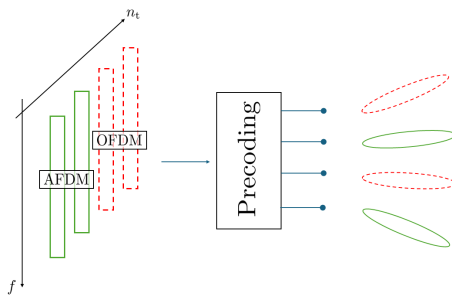


FIGURE 11: Spatial coexistence in MIMO-AFDM systems utilizing digital beamforming ($N_t = 4$).

F. Phase Noise and Carrier Frequency Offset

PHN and carrier frequency offset (CFO) represent two primary hardware impairments stemming from the non-idealities of practical local oscillators (LOs) [108], [109]. In modern broadband systems, especially those operating at higher carrier frequencies, LOs are susceptible to thermal and flicker noise-induced instabilities. These imperfections manifest as random phase drifts and frequency deviations that distort the baseband waveform during up-conversion and down-conversion. While these effects are highly detrimental to OFDM, which relies on precise time-frequency alignment, the chirped subcarriers of AFDM offer an inherent structural resilience to these distortions [110].

1) Characterization of PHN and CFO

To characterize the statistical behavior of PHN, a discrete-time Wiener process model is typically employed [111], [112]. In this framework, the Gaussian PHN increments $\Delta[n]$ at a given antenna evolve as

$$\varphi[n] = \varphi[n - 1] + \Delta[n], \quad n = 1, \dots, N - 1, \quad (90)$$

where $\Delta[n]$ is a zero-mean Gaussian process with variance $\sigma_\Delta^2 = 4\pi^2 f_c^2 \xi T_s$, and ξ represents the oscillator quality and T_s denotes the sampling period [113].

Given the above, the resulting distortion is modeled by the diagonal PHN matrix as

$$\Theta = \text{diag} \{ e^{j\varphi[0]}, \dots, e^{j\varphi[N-1]} \}. \quad (91)$$

The spatial correlation of PHN is determined by the LO architecture. In co-located MIMO arrays, a common local oscillator (CLO) is typically utilized, resulting in identical PHN across all antenna elements. Conversely, distributed or RF-chain-per-antenna architectures employ separate local oscillators (SLOs), leading to spatially independent phase fluctuations. This distinction is critical, as CLO induces coherent distortion, whereas SLOs can significantly degrade beamforming gains and the accuracy of spatial parameter estimation [114].

CFO arises from frequency mismatches between the transmit and receive LOs, which are inevitable due to hardware tolerances and temperature variations. This mismatch induces a linearly increasing phase rotation across the time-domain samples. In multi-carrier systems, this destroys subcarrier orthogonality, leading to severe ICI. For chirp-based AFDM, CFO manifests as an additional Doppler-like phase rotation, characterized by the diagonal matrix [54], [107]

$$\mathbf{P} = \text{diag} \{ 1, e^{j2\pi\theta_{\text{CFO}}/N}, \dots, e^{j2\pi\theta_{\text{CFO}}(N-1)/N} \}, \quad (92)$$

where θ_{CFO} represents the normalized CFO factor.

In all, incorporating the impairments, the effective channel matrix from (56) is generalized as

$$\mathbf{H} = \Theta \mathbf{P} \left(\sum_{p=1}^P h_p \cdot \Phi_p \cdot \mathbf{V}^{f_p} \cdot \mathbf{\Pi}^{\ell_p} \right). \quad (93)$$

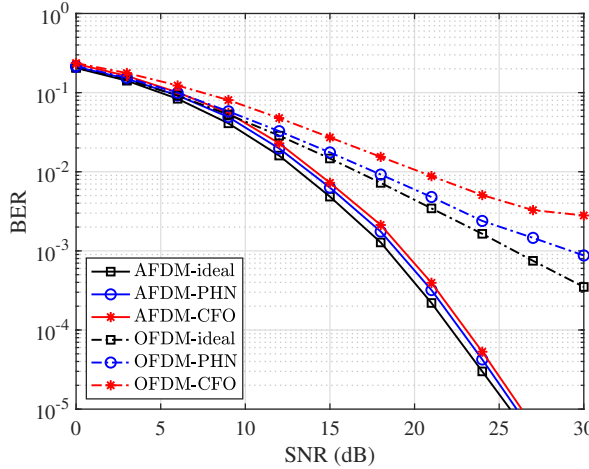


FIGURE 12: BER performance of OFDM/AFDM under PHN and CFO impairments ($N=128$, QPSK, $\theta_{\text{CFO}} = \frac{1}{10}$, $P=3$), with LMMSE detection.

2) Waveform Resilience and Performance

The impact of PHN and CFO differs fundamentally between the two waveforms due to their distinct basis functions. In OFDM, these impairments disrupt the frequency-domain orthogonality, manifesting as a common phase error (CPE) and rapidly varying ICI that scales with the magnitude of the CFO. Consequently, OFDM requires highly accurate tracking and compensation to prevent severe bit error rate (BER) degradation.

In contrast, AFDM utilizes DAFT-domain chirps that sweep across the time-frequency plane. This structure provides frequency diversity, as the symbol energy is spread across multiple frequency components. The phase rotation induced by CFO partially aligns with the intrinsic linear chirp slope, rendering AFDM significantly more tolerant to moderate CFO levels compared to the static sinusoidal subcarriers of the conventional OFDM.

Numerical evaluations of BER performance, as shown in Fig. 12, confirm these characteristics. Using $N = 128$ subcarriers, quadrature phase shift keying (QPSK) modulation, and $\theta_{\text{CFO}} = 0.1$, it is observed that AFDM performance remains nearly identical to the ideal (impairment-free) case. Conversely, at a BER of 3×10^{-3} , OFDM exhibits signal-to-noise ratio (SNR) losses of approximately 2 dB due to PHN and 8 dB due to CFO. Furthermore, in PHN scenarios at a BER of 10^{-3} , AFDM achieves a significant gain of 10.5 dB over OFDM, demonstrating superior robustness to oscillator non-idealities.

G. Degrees of Freedom via the Chirp Parameter Domain

The parameterizable nature of the DAFT, in its two chirp parameters λ_1 and λ_2 , allows AFDM to adapt its signal structure to specific system requirements beyond conventional data transmission. In addition to tuning the parameters for pure robustness and diversity objective, this

flexibility can also be exploited to implement advanced functionalities such as index modulation (IM), physical layer security (PLS), and PAPR reduction.

It is essential to note that these functionalities can be implemented without altering the fundamental AFDM framework, thus preserving its inherent advantages in doubly dispersive channels, and are not possible with any other waveforms such as OFDM and OTFS, due to the lack of such flexibly tunable parameters.

1) Index Modulation

IM schemes originally proposed for OFDM [115], [116] has also been effectively adapted to the AFDM framework [33], [117]. This technique involves partitioning N subcarriers into K_{IM} subsets, each containing $N_{\text{IM}} = \frac{N}{K_{\text{IM}}}$ subcarriers, and in each subset, $m_{\text{IM}} < N_{\text{IM}}$ subcarriers are selected as active, while the remaining $N_{\text{IM}} - m_{\text{IM}}$ indices are left inactive. Consequently, binary information is conveyed not only through the M -ary complex symbols but also through the selection of active indices, as also extensively studied in other IM literature such as spatial modulation (SM) [118]–[120] and STSK [121] for MIMO systems. More recently, by using additional bits to select the active transmit antennas, the GSM-aided AFDM scheme has been studied in [89].

The IM spectral efficiency (in bps) of is given by

$$R_{\text{IM}} = K_{\text{IM}} \cdot \log_2 \left(\left\lceil \binom{N_{\text{IM}}}{m_{\text{IM}}} \right\rceil \right) + K_{\text{IM}} m_{\text{IM}} \cdot \log_2(M), \quad (94)$$

offering improved BER performance or spectral efficiency compared to standard AFDM [122].

From a structural perspective, AFDM-IM represents an evolution of OFDM-IM where the modulation is performed in the DAFT domain rather than the frequency domain. This backward compatibility allows the adaptation of various OFDM-IM enhancements, such as subcarrier power modulation [123] and multi-mode signaling [124], [125].

Beyond standard subcarrier selection, AFDM introduces unique dimensions for IM through its parameterizable chirp structure. For instance, the chirp parameter λ_2 can be dynamically selected from a finite set for each subcarrier subset, effectively increasing the aggregate bit rate without requiring additional bandwidth [34].

Alternatively, information can be conveyed via the permutation of the chirp sequences themselves, a technique known as *chirp-permutation* IM (CP-IM) [35], [126]. This approach has been shown to provide significant performance gains while maintaining a complete set of active subcarriers, thereby avoiding the spectral efficiency loss typically associated with traditional IM schemes.

2) Physical Layer Security

PLS leverages the physical dimensions of the communication system, such as time, frequency, and chirp parameters, to complement higher-layer encryption. AFDM offers a unique paradigm for PLS centered on the tunability of (λ_1, λ_2) .

Research indicates that AFDM can achieve near-perfect security by utilizing permutations over chirp sequences [38], [126], creating a combinatorial complexity that remains resilient even against quantum-accelerated eavesdropping attempts. In addition analytical results also demonstrate that AFDM provides superior PLS compared to OTFS and OFDM, as measured by the brute-force complexity required for unauthorized demodulation [36]. Furthermore, parameter-hopping schemes for (λ_1, λ_2) can be implemented to dynamically vary the waveform characteristics [37], [127]–[129]. Combined with its inherent robustness against jamming and eavesdropping due to its wideband chirp nature [36], [130], AFDM stands as a highly secure waveform.

3) PAPR Reduction

As AFDM is constructed from a summation of subcarriers, it exhibits a PAPR profile statistically similar to that of OFDM, whereas OTFS typically achieves lower values [28], [126]. However, this similarity is a significant advantage for system reusability. Legacy OFDM PAPR reduction techniques such as clipping, μ -law companding [131], and data precoding [132] are directly applicable to AFDM, allowing for the reuse of established hardware infrastructure, including PA linearization and digital front-end processing.

Beyond legacy methods, specific AFDM PAPR reduction strategies have recently emerged. These include pre-chirp selection, where λ_2 is optimized within a finite set to minimize the peak power for each block [133], and the use of block-diagonal DFTs pre-chirp matrices [134], [135].

V. Reusability of AFDM with respect to OFDM

To summarize the technical analysis, this section qualitatively evaluates the reusability of AFDM with the established OFDM legacy. This assessment is pivotal

for 6G standardization, where minimizing infrastructure replacement costs is as critical as performance gains.

A detailed breakdown of this compatibility is presented in Table 2. In the **RF and Analog** domain, the waveform's statistical similarity to OFDM allows for the **direct reuse** of power amplifiers and transceivers without redesign. In the **PHY Layer**, while the core FFT hardware accelerators are preserved, the transition primarily necessitates **software updates** for channel estimation logic and phase rotation (chirping). Finally, compatible **MAC** integration is achieved through minimal **extensions** to existing structure and control signaling, validating AFDM as a high-performance yet low-risk evolutionary candidate for 6G+.

VI. Conclusion

In this work, we demonstrated that AFDM is a uniquely balanced waveform candidate for 6G+ wireless systems, bridging the gap between the performance requirements of extreme-mobility scenarios and the practical demand for hardware reusability. By highlighting the construction of the AFDM framework upon the established OFDM legacy, we have shown that high-fidelity communications in doubly dispersive channels can be achieved with a modular, evolutionary approach rather than a radical system redesign.

The presented analysis confirms that AFDM exhibits exceptional reusability in the RF front-end and at the receiver. Furthermore, the tunable chirp-parameter domain of AFDM offers new degrees of freedom for secondary functionalities, including IM, PLS, and sensing, while maintaining compatibility with legacy resource grids.

In a nutshell, AFDM offers a low-risk, high-reward waveform candidate for 6G standardization and beyond, preserving the engineering investments of previous generations while meeting the stringent demands of the future wireless landscape.

TABLE 2: Reusability Analysis: AFDM against the OFDM Legacy Infrastructure

Domain	Module / Function	Reusability	Architectural Impact & Rationale
RF & Analog	RF Chain (<i>PA, Antennas, Cabling</i>)	Direct Reuse	AFDM retains the statistical PAPR distribution and spectral mask of OFDM. No new power back-off, PA linearization, or antenna/cable redesign is required. Sampling rates, quantization noise floors, and dynamic range requirements remain identical to standard OFDM.
	Mixed Signal (<i>ADC / DAC</i>)	Direct Reuse	
PHY Layer	FFT / IFFT Engines	Direct Reuse	The core butterfly accelerators are preserved. AFDM is implemented as a wrapper around the legacy OFDM block.
	Waveform Generation	Soft Update	Requires insertion of two element-wise phase rotation vectors digitally (pre/post-chirp) at $\mathcal{O}(N)$ complexity.
	Channel Estimation / Equalization	Logic Update	Requires new algorithms for the additional Doppler-domain recovery and equalization (in DAFT domain). Standard estimators (LS/MMSE) must be upgraded, or alternate novel estimators can be used.
MAC & Control	Pilot Structure	Adaptable	Legacy one-dimensional time-domain pilot placement and padding are reusable, but optimal performance in high mobility may require different placement within total time-frequency grid and chirp-aware wrapping.
	Resource Grid	Compatible	Resources map to 1D streams. The fundamental time-frequency resource element (RE) grid structure is preserved.
	Control Signaling (DCI)	Extension	Standard downlink control information (DCI) formats can apply, but new chirp parameters (chirp indices) may require additional signaling bits.

VII. Use of AI Tools

Generative AI tools, including ChatGPT, Gemini, and Copilot, were utilized in this work for editorial refinement, code optimization, and literature scoping. These tools served only as auxiliary instruments to enhance clarity and presentation, and they did not generate new scientific concepts or results. The authors have carefully verified all AI-assisted content and assume full responsibility for the accuracy, integrity, and originality of the manuscript.

REFERENCES

- [1] S. Dang *et al.*, “What should 6G be?” *Nature Electronics*, vol. 3, no. 1, pp. 20–29, 2020.
- [2] W. Jiang *et al.*, “The road towards 6G: A comprehensive survey,” *IEEE Open Journal of the Communications Society*, vol. 2, pp. 334–366, 2021.
- [3] C. X. Wang *et al.*, “On the road to 6G: Visions, requirements, key technologies, and testbeds,” *IEEE Communications Surveys & Tutorials*, vol. 25, no. 2, pp. 905–974, 2023.
- [4] 3GPP TSG RAN, “R1-21508043: Feature Lead summary #3 on 6G waveform (Source: Nokia), RAN1 Meeting #122bis,” Oct. 2025.
- [5] 3GPP, Group Services and System Aspects, “TR 22.870: Study on 6G Use Cases and Service Requirements,” Jun. 2025, Release 20, v0.3.1.
- [6] 3GPP TSG RAN, “RP-251881: New SID: Study on 6G Radio,” Jun. 2025, RAN Meeting #108.
- [7] X. Lin *et al.*, “5G New Radio: Unveiling the Essentials of the Next Generation Wireless Access Technology,” *IEEE Communications Standards Magazine*, vol. 3, no. 3, pp. 30–37, 2019.
- [8] E. Dahlman, S. Parkvall, and J. Skold, *5G NR: The next generation wireless access technology*. Academic Press, 2020.
- [9] 3GPP, “Evolved universal terrestrial radio access (E-UTRA); physical channels and modulation,” 3rd Generation Partnership Project (3GPP), Technical Specification (TS) TS 36.211, 2008.
- [10] 3GPP, “NR; physical channels and modulation,” 3rd Generation Partnership Project (3GPP), Technical Specification (TS) TS 38.211, 2018.
- [11] M. Morelli, C.-C. J. Kuo, and M.-O. Pun, “Synchronization techniques for orthogonal frequency division multiple access (OFDMA): A tutorial review,” *Proceedings of the IEEE*, vol. 95, no. 7, pp. 1394–1427, 2007.
- [12] S. H. Han and J. H. Lee, “An overview of peak-to-average power ratio (PAPR) reduction techniques for multicarrier transmission,” *IEEE wireless communications*, vol. 12, no. 2, pp. 56–65, 2005.
- [13] M. Ozdemir and H. Arslan, “Channel estimation for wireless OFDM systems,” *IEEE Communications Surveys & Tutorials*, vol. 9, no. 2, 2007.
- [14] Y. Liu *et al.*, “Channel estimation for OFDM,” *IEEE Communications Surveys & Tutorials*, vol. 16, no. 4, pp. 1891–1908, 2014.
- [15] W. Saad, M. Bennis, and M. Chen, “A Vision of 6G Wireless Systems: Applications, Trends, Technologies, and Open Research Problems,” *IEEE Network*, vol. 34, no. 3, pp. 134–142, 2020.
- [16] D. Bliss and S. Govindasamy, *Dispersive and doubly dispersive channels*. Cambridge University Press, 2013.
- [17] V. Koivunen *et al.*, “Multicarrier ISAC: Advances in waveform design, signal processing, and learning under nonidealities,” *IEEE Signal Processing Magazine*, vol. 41, no. 5, pp. 17–30, 2024.
- [18] M. Harounabadi and T. Heyn, “Toward integration of 6G-NTN to terrestrial mobile networks: Research and standardization aspects,” *IEEE Wireless Communications*, vol. 30, no. 6, pp. 20–26, 2023.
- [19] G. Araniti *et al.*, “Toward 6G non-terrestrial networks,” *IEEE Network*, vol. 36, no. 1, pp. 113–120, 2021.
- [20] M. Gismalla *et al.*, “Survey on device to device (D2D) communication for 5G/6G networks: Concept, applications, challenges, and future directions,” *IEEE Access*, vol. 10, pp. 30792–30821, 2022.
- [21] M. Noor-A-Rahim *et al.*, “6G for vehicle-to-everything (V2X) communications: Enabling technologies, challenges, and opportunities,” *Proceedings of the IEEE*, vol. 110, no. 6, pp. 712–734, 2022.
- [22] D. Mishra *et al.*, “Drone networking in the 6G era: A technology overview,” *IEEE Communications Standards Magazine*, vol. 5, no. 4, pp. 88–95, 2022.
- [23] T. Wang *et al.*, “Performance degradation of OFDM systems due to doppler spreading,” *IEEE Trans. Wireless Commun.*, vol. 5, no. 6, pp. 1422–1432, 2006.
- [24] F. Liu *et al.*, “Integrated Sensing and Communications: Toward Dual-Functional Wireless Networks for 6G and Beyond,” *IEEE J. Sel. Area. Comm.*, vol. 40, no. 6, pp. 1728–1767, 2022.
- [25] Z. Wei *et al.*, “Integrated sensing and communication signals toward 5G-A and 6G: A survey,” *IEEE Internet Things J.*, vol. 10, no. 13, pp. 11068–11092, 2023.
- [26] T. Wild, V. Braun, and H. Viswanathan, “Joint design of communication and sensing for beyond 5G and 6G systems,” *IEEE Access*, vol. 9, pp. 30845–30857, 2021.
- [27] S. D. Liyanaarachchi *et al.*, “Optimized waveforms for 5G-6G communication with sensing: Theory, simulations and experiments,” *IEEE Trans. Wireless Commun.*, vol. 20, no. 12, pp. 8301–8315, 2021.
- [28] H. S. Rou *et al.*, “From Orthogonal Time-Frequency Space to Affine Frequency-Division Multiplexing: A comparative study of next-generation waveforms for integrated sensing and communications in doubly dispersive channels,” *IEEE Signal Processing Magazine*, vol. 41, no. 5, pp. 71–86, 2024.
- [29] A. Bemani, N. Ksairi, and M. Kountouris, “Affine Frequency Division Multiplexing for Next Generation Wireless Communications,” *IEEE Trans. Wireless Commun.*, vol. 22, no. 11, pp. 8214–8229, 2023.
- [30] H. S. Rou *et al.*, “Affine frequency division multiplexing (AFDM) for 6G: Properties, features, and challenges,” *IEEE Communications Standards Magazine*, pp. 1–10, 2025.
- [31] H. Yin *et al.*, “Affine frequency division multiplexing: Extending OFDM for scenario-flexibility and resilience,” *arXiv preprint arXiv:2502.04735*, 2025.
- [32] Q. Li *et al.*, “Affine frequency division multiplexing for 6G networks: Fundamentals, opportunities, and challenges,” *IEEE Network*, 2025.
- [33] Y. Tao *et al.*, “Affine Frequency Division Multiplexing With Index Modulation: Full Diversity Condition, Performance Analysis, and Low-Complexity Detection,” *IEEE J. Sel. Area. Comm.*, vol. 43, no. 4, pp. 1041–1055, April 2025.
- [34] G. Liu *et al.*, “Pre-chirp-domain index modulation for full-diversity affine frequency division multiplexing toward 6G,” *IEEE Trans. Wireless Commun.*, vol. 24, no. 9, pp. 7331–7345, September 2025.
- [35] H. S. Rou *et al.*, “AFDM chirp-permutation-index modulation with quantum-accelerated codebook design,” in *2024 58th Asilomar Conference on Signals, Systems, and Computers*, 2024, pp. 817–821.
- [36] V. Savaux *et al.*, “On the Robustness of AFDM and OTFS Against Passive Eavesdroppers,” *IEEE Wireless Commun. Lett.*, pp. 1–1, 2026.
- [37] P. Wang *et al.*, “A Secure Affine Frequency Division Multiplexing for Wireless Communication Systems,” in *Proc. IEEE ICC*, 2025, pp. 2701–2706.
- [38] H. S. Rou and G. T. F. de Abreu, “Chirp-permuted AFDM for quantum-resilient physical-layer secure communications,” *IEEE Wireless Commun. Lett.*, pp. 1–1, 2025.
- [39] Y. Liu *et al.*, “DFT-s-OFDM with chirp modulation,” in *2025 IEEE 36th International Symposium on Personal, Indoor and Mobile Radio Communications (PIMRC)*, 2025, pp. 1–6.
- [40] M. Ahmad *et al.*, “Radar-centric AFDM waveform with chirp-domain index modulation for ISAC,” *IEEE Open Journal of the Communications Society*, vol. 7, pp. 844–857, 2026.
- [41] Z. Sui *et al.*, “Multi-functional chirp signalling for next-generation multi-carrier wireless networks: Communications, sensing and ISAC perspectives,” *arXiv preprint arXiv:2508.06022*, 2025.
- [42] S. Sabuj, S.-H. Lee, and H.-S. Jo, “A complex wavelet AFDM scheme for integrated sensing and communication in LEO satellite,” *Authorea Preprints*, 2025.
- [43] K. R. R. *et al.*, “Affine filter bank modulation (AFBM): A novel 6G ISAC waveform with low PAPR and OOBE,” *arXiv preprint arXiv:2509.05683*, 2025.
- [44] Q. Yi *et al.*, “Non-orthogonal affine frequency division multiplexing for spectrally efficient high-mobility communications,” *arXiv preprint arXiv:2508.09782*, 2025.
- [45] H. L. Senger *et al.*, “Affine filter bank modulation: A new waveform for high mobility communications,” *arXiv preprint arXiv:2505.03589*, 2025.

[46] Z. Wei *et al.*, "Orthogonal Time-Frequency Space Modulation: A Promising Next-Generation Waveform," *IEEE Wireless Communications*, vol. 28, no. 4, pp. 136–144, 2021.

[47] T. Thaj and E. Viterbo, "Orthogonal time sequence multiplexing modulation," in *2021 IEEE Wireless Communications and Networking Conference (WCNC)*, 2021, pp. 1–7.

[48] Z. Sui *et al.*, "Performance analysis and approximate message passing detection of orthogonal time sequence multiplexing modulation," *IEEE Trans. Wireless Commun.*, vol. 23, no. 3, pp. 1913–1928, 2024.

[49] H. Lin and J. Yuan, "Orthogonal delay-doppler division multiplexing modulation," *IEEE Trans. Wireless Commun.*, vol. 21, no. 12, pp. 11 024–11 037, 2022.

[50] F. Lampel, A. Avarado, and F. M. Willems, "On OTFS using the discrete zak transform," in *2022 IEEE International Conference on Communications Workshops (ICC Workshops)*. IEEE, 2022, pp. 729–734.

[51] Y. Hong, T. Thaj, and E. Viterbo, *Delay-Doppler Communications: Principles and Applications*. Academic Press, 2022.

[52] S. Li *et al.*, "Performance analysis of coded OTFS systems over high-mobility channels," *IEEE Trans. Wireless Commun.*, vol. 20, no. 9, pp. 6033–6048, 2021.

[53] G. D. Surabhi, R. M. Augustine, and A. Chockalingam, "On the diversity of uncoded OTFS modulation in doubly-dispersive channels," *IEEE Trans. Wireless Commun.*, vol. 18, no. 6, pp. 3049–3063, 2019.

[54] A. Bemani, G. Cuozzo, N. Ksairi, and M. Kountouris, "Affine Frequency Division Multiplexing for Next-Generation Wireless Networks," in *2021 17th International Symposium on Wireless Communication Systems (ISWCS)*, October 2021, pp. 1–6.

[55] A. Bemani, N. Ksairi, and M. Kountouris, "Integrated sensing and communications with affine frequency division multiplexing (AFDM)," *IEEE Wireless Commun. Lett.*, vol. 13, no. 5, pp. 1255–1259, 2024.

[56] Y. Ni, Z. Wang, P. Yuan, and Q. Huang, "An AFDM-based integrated sensing and communications," in *2022 International Symposium on Wireless Communication Systems (ISWCS)*. IEEE, 2022, pp. 1–6.

[57] Y. Luo, Y. L. Guan, Y. Ge, and C. Yuen, "Target sensing with off-grid sparse bayesian learning for AFDM-ISAC system," *arXiv preprint arXiv:2503.10011*, 2025.

[58] Y. Ni *et al.*, "An integrated sensing and communications system based on affine frequency division multiplexing," *IEEE Trans. Wireless Commun.*, 2025.

[59] Y. Luo *et al.*, "A novel angle-delay-doppler estimation scheme for AFDM-ISAC system in mixed near-field and far-field scenarios," *IEEE Internet Things J.*, 2025.

[60] H. S. Rou and G. T. F. de Abreu, "Normalized ambiguity function characteristics of OFDM, OTFS, AFDM, and CP-AFDM for ISAC," *Accepted at the IEEE ICC 2026, preprint available arXiv:2510.11216*, 2025.

[61] Y. Ni *et al.*, "Ambiguity function analysis of AFDM under pulse-shaped random ISAC signaling," *arXiv preprint arXiv:2511.04200*, 2025.

[62] J. Zhu *et al.*, "AFDM-based bistatic integrated sensing and communication in static scatterer environments," *IEEE Wireless Commun. Lett.*, vol. 13, no. 8, pp. 2245–2249, 2024.

[63] J. Zhu *et al.*, "ISAC with affine frequency division multiplexing: An FMCW-based signal processing perspective," *arXiv preprint arXiv:2511.12308*, 2025.

[64] F. Zhang *et al.*, "AFDM-enabled integrated sensing and communication: Theoretical framework and pilot design," *arXiv preprint arXiv:2502.14203*, 2025.

[65] Y. Luo *et al.*, "AFDM-enabled integrated sensing and communication for 4D reconstruction," in *2025 5th International Conference on Intelligent Communications and Computing (ICICC)*. IEEE, 2025, pp. 211–216.

[66] K. Ramadan, A. A. Alharbi, and E. S. Hassan, "Performance evaluation of AFDM for integrated sensing and communications in doubly dispersive channels," *Defence Technology*, 2026.

[67] X. Ouyang and J. Zhao, "Orthogonal Chirp Division Multiplexing," *IEEE Trans. Commun.*, vol. 64, no. 9, pp. 3946–3957, 2016.

[68] Z. Gong *et al.*, "Channel estimation, interpolation and extrapolation in doubly-dispersive channels," *arXiv preprint arXiv:2408.09381*, 2024.

[69] K. R. R. Ranasinghe *et al.*, "Doubly-dispersive continuous MIMO systems: Channel modeling and beamforming design," *arXiv preprint arXiv:2509.00964*, 2025.

[70] K. R. R. Ranasinghe *et al.*, "Doubly-dispersive MIMO channels with stacked intelligent metasurfaces: Modeling, parametrization, and receiver design," *IEEE Transactions on Wireless Communications*, vol. 25, pp. 3801–3817, 2026.

[71] K. R. R. Ranasinghe *et al.*, "Flexible intelligent metasurfaces in high-mobility MIMO integrated sensing and communications," *arXiv preprint arXiv:2507.18793*, 2025.

[72] R. W. Bäuml, R. F. H. Fischer, and J. B. Huber, "Reducing the peak-to-average power ratio of multicarrier modulation by selected mapping," *Electronics Letters*, vol. 32, no. 22, pp. 2056–2057, 1996.

[73] 3GPP TS 36.211 V17.2.0: *Evolved Universal Terrestrial Radio Access (E-UTRA); Physical Channels and Modulation*, 3rd Generation Partnership Project (3GPP) Std., 2023, release 17. [Online]. Available: https://www.3gpp.org/ftp/Specs/archive/36_series/36.211/36211-g20.zip

[74] IEEE Std 802.11-2012: *Wireless LAN Medium Access Control (MAC) and Physical Layer (PHY) Specifications*, IEEE Std., 2012, clause 18.3.5.8: Pilot Subcarriers and Polarity Sequence.

[75] ETSI EN 300 744 V1.6.1: *Digital Video Broadcasting (DVB); Framing Structure, Channel Coding and Modulation for Digital Terrestrial Television*, European Telecommunications Standards Institute (ETSI) Std., 2009, clause 4.6.2: Pilot Modulation Using PRBS. [Online]. Available: https://www.etsi.org/deliver/etsi_en/300700_300799/300744/01.06.01_60/en_300744v010601p.pdf

[76] H. Yin, Y. Tang, S. Li, Y. Zhou, and C. Yi, "Evaluation and design criterion for pulse-shaped AFDM," in *GLOBECOM 2024 - 2024 IEEE Global Communications Conference*, 2024, pp. 4944–4949.

[77] M. Mirabella, P. D. Viesti, and G. M. Vitetta, "On the use of a two-dimensional cyclic prefix in OTFS modulation and its implications," *IEEE Open Journal of the Communications Society*, vol. 5, pp. 3340–3367, 2024.

[78] M. Mirabella, P. Di Viesti, and G. M. Vitetta, "Implementation of an OTFS-DCP-based communication system on software-defined radios," in *2025 IEEE Wireless Communications and Networking Conference (WCNC)*, 2025, pp. 1–7.

[79] H. Yin and Y. Tang, "Pilot Aided Channel Estimation for AFDM in Doubly Dispersive Channels," in *2022 IEEE/CIC International Conference on Communications in China (ICCC)*, August 2022, pp. 308–313.

[80] Y. Zhou *et al.*, "GI-Free Pilot-Aided Channel Estimation for Affine Frequency Division Multiplexing Systems," 2024. [Online]. Available: <https://arxiv.org/abs/2404.01088>

[81] K. Zheng *et al.*, "Channel Estimation for AFDM With Superimposed Pilots," *IEEE Trans. Veh. Technol.*, vol. 74, no. 2, pp. 3389–3394, February 2025.

[82] V. Savaux, "Pilot design for multiple domains channel estimation in special cases of affine frequency division multiplexing," *Physical Communication*, vol. 73, p. 102863, December 2025. [Online]. Available: <https://www.sciencedirect.com/science/article/pii/S1874490725002666>

[83] V. Savaux, "Special Cases of DFT-Based Modulation and Demodulation for Affine Frequency Division Multiplexing," *IEEE Trans. Commun.*, vol. 72, no. 12, pp. 7627–7638, 2024.

[84] 3GPP, "Physical channels and modulation," 3GPP, Tech. Rep. TS 38.211 v16.2.0, July 2020.

[85] S. Coleri, M. Ergen, A. Puri, and A. Bahai, "A Study of Channel Estimation in OFDM Systems," in *Vehicular Technology Conference*, vol. 2, september 2002, pp. 894–898.

[86] V. Savaux and Y. Louët, "LMMSE channel estimation in OFDM context: a review," *IET Signal Processing*, vol. 11, no. 2, pp. 123–134, April 2017.

[87] C. Shen, J. Yuan, and J. Tong, "Time-domain zero-padding (TZP) AFDM with two-stage iterative MMSE detection," *IEEE Trans. Wireless Commun.*, pp. 1–1, 2025.

[88] H. Hawkins, C. Xu, L.-L. Yang, and L. Hanzo, "Iterative soft-MMSE detection aided AFDM and OTFS," *IEEE Open J. Veh. Technol.*, vol. 6, pp. 2944–2959, 2025.

[89] Z. Sui *et al.*, "Generalized spatial modulation aided affine frequency division multiplexing," *IEEE Trans. Wireless Commun.*, pp. 1–16, 2025.

[90] Z. Li *et al.*, “Chirp parameter selection for affine frequency division multiplexing with MMSE equalization,” *IEEE Trans. Commun.*, vol. 73, no. 7, pp. 5079–5093, 2025.

[91] S. Tiwari, S. S. Das, and V. Rangamgari, “Low complexity LMMSE receiver for OTFS,” *IEEE Commun. Lett.*, vol. 23, no. 12, pp. 2205–2209, 2019.

[92] Q. Yi, Z. Sui, and Z. Liu, “Error rate analysis and low-complexity receiver design for zero-padded AFDM,” *arXiv preprint arXiv:2510.14507*, 2025.

[93] L. Rugini, P. Banelli, and G. Leus, “Simple equalization of time-varying channels for OFDM,” *IEEE Commun. Lett.*, vol. 9, no. 7, pp. 619–621, 2005.

[94] A. Bemani, N. Ksairi, and M. Kountouris, “Low complexity equalization for AFDM in doubly dispersive channels,” in *Proc. IEEE ICASSP*, 2022, pp. 5273–5277.

[95] Q. Luo *et al.*, “AFDM-SCMA: A promising waveform for massive connectivity over high mobility channels,” *IEEE Trans. Wireless Commun.*, vol. 23, no. 10, pp. 14421–14436, 2024.

[96] X. Li *et al.*, “Affine frequency division multiplexing over wideband doubly-dispersive channels with time-scaling effects,” *IEEE Trans. Wireless Commun.*, pp. 1–1, 2025.

[97] L. Wu *et al.*, “AFDM signal detection based on message passing scheme,” *Digital Signal Processing*, vol. 153, p. 104633, 2024.

[98] K. R. R. Ranasinghe *et al.*, “Joint channel, data, and radar parameter estimation for AFDM systems in doubly-dispersive channels,” *IEEE Trans. Wireless Commun.*, vol. 24, no. 2, pp. 1602–1619, 2025.

[99] Y. Xu *et al.*, “AFDM-aided grant-free random access for LEO SIoT: Performance analysis and near-optimal joint detection,” *IEEE Trans. Commun.*, pp. 1–1, 2025.

[100] Q. Luo *et al.*, “Joint sparse graph for enhanced MIMO-AFDM receiver design,” *IEEE Trans. Wireless Commun.*, pp. 1–1, 2025.

[101] M. Tuchler, A. C. Singer, and R. Koetter, “Minimum mean squared error equalization using *a priori* information,” *IEEE Trans. Signal Process.*, vol. 50, no. 3, pp. 673–683, 2002.

[102] H. Yin, X. Wei, Y. Tang, and K. Yang, “Diagonally Reconstructed Channel Estimation for MIMO-AFDM With Inter-Doppler Interference in Doubly Selective Channels,” *IEEE Trans. Wireless Commun.*, vol. 23, no. 10, pp. 14 066–14 079, October 2024.

[103] V. Savaux and X. Chen, “Spatial Precoding in Frequency Domain for Multi-User MIMO Affine Frequency Division Multiplexing,” in *Proc. IEEE EUSIPCO*, August 2024, pp. 2112–2116.

[104] R. Y. Bir, A. A. Boudjelal, and H. Arslan, “On the orthogonal coexistence of AFDM and OFDM for joint sensing and communication,” *IEEE Open J. Commun. Soc.*, vol. 6, pp. 10 010–10 022, November 2025.

[105] K. Abela, S. Abidrabbu, A. A. Boudjelal, and H. Arslan, “Waveform coexistence-driven RSMA: A pioneering strategy for future 6G networks,” *arXiv preprint https://arxiv.org/abs/2505.18739*, 2025.

[106] Y. Yin *et al.*, “Downlink AFDM-RSMA scheme based on orthogonal chirps and sum-rate maximization,” in *2025 IEEE/CIC International Conference on Communications in China (ICCC)*. IEEE, 2025, pp. 1–6.

[107] H. Liu *et al.*, “BER analysis of SCMA-OFDM systems in the presence of carrier frequency offset,” *IEEE Commun. Lett.*, vol. 28, no. 1, pp. 213–217, Jan. 2024.

[108] L. Piazza and P. Mandarini, “Analysis of phase noise effects in OFDM modems,” *IEEE Trans. Commun.*, vol. 50, no. 10, pp. 1696–1705, Oct. 2002.

[109] H. Mehrpouyan *et al.*, “Joint estimation of channel and oscillator phase noise in MIMO systems,” *IEEE Trans. Signal Process.*, vol. 60, no. 9, pp. 4790–4807, Sep. 2012.

[110] Z. Sui *et al.*, “MIMO-AFDM outperforms MIMO-OFDM in the face of hardware impairments,” *arXiv preprint arXiv:2601.00502*, 2026.

[111] D. D. Lin and T. J. Lim, “The variational inference approach to joint data detection and phase noise estimation in OFDM,” *IEEE Trans. Signal Process.*, vol. 55, no. 5, pp. 1862–1874, May 2007.

[112] R. Wang, H. Mehrpouyan, M. Tao, and Y. Hua, “Channel estimation, carrier recovery, and data detection in the presence of phase noise in OFDM relay systems,” *IEEE Trans. Wireless Commun.*, vol. 15, no. 2, pp. 1186–1205, 2016.

[113] Z. Sui, H. Q. Ngo, M. Matthaiou, and L. Hanzo, “Performance analysis and optimization of STAR-RIS-aided cell-free massive MIMO systems relying on imperfect hardware,” *IEEE Trans. Wireless Commun.*, vol. 24, no. 4, pp. 2925–2939, Apr. 2025.

[114] E. Björnson, M. Matthaiou, and M. Debbah, “Massive MIMO with non-ideal arbitrary arrays: Hardware scaling laws and circuit-aware design,” *IEEE Trans. Wireless Commun.*, vol. 14, no. 8, pp. 4353–4368, Apr. 2015.

[115] E. Başar *et al.*, “Orthogonal frequency division multiplexing with index modulation,” *IEEE Trans. Signal Process.*, vol. 61, no. 22, pp. 5536–5549, 2013.

[116] Z. Sui *et al.*, “Approximate message passing algorithms for low complexity OFDM-IM detection,” *IEEE Trans. Veh. Technol.*, vol. 70, no. 9, pp. 9607–9612, 2021.

[117] Y. Tao, M. Wen, Y. Ge, and J. Li, “Affine Frequency Division Multiplexing With Index Modulation,” in *Proc. IEEE WCNC*, April 2024, pp. 1–6.

[118] R. Y. Mesleh *et al.*, “Spatial modulation,” *IEEE Trans. Veh. Technol.*, vol. 57, no. 4, pp. 2228–2241, 2008.

[119] H. S. Rou *et al.*, “Scalable Quadrature Spatial Modulation,” *IEEE Transactions on Wireless Communications*, vol. 21, no. 11, pp. 9293–9311, Nov. 2022.

[120] Z. Sui *et al.*, “Low complexity detection of spatial modulation aided OTFS in doubly-selective channels,” *IEEE Trans. Veh. Technol.*, vol. 72, no. 10, pp. 13 746–13 751, 2023.

[121] Z. Sui *et al.*, “Space-time shift keying aided OTFS modulation for orthogonal multiple access,” *IEEE Trans. Commun.*, vol. 71, no. 12, pp. 7393–7408, 2023.

[122] J. Zhu *et al.*, “Design and performance analysis of index modulation empowered AFDM system,” *IEEE Wireless Commun. Lett.*, vol. 13, no. 3, pp. 686–690, 2024.

[123] M. Temiz and C. Masouros, “Affine Frequency Division Multiplexing with Subcarrier Power-Level Index Modulation for Integrated Sensing and Communications,” June 2025.

[124] A. A., C. K. Thomas, K. S., J. B. Benifa, and W. Saad, “Dual-mode Index Modulation based on Affine Frequency Division Multiplexing,” *Physical Communication*, vol. 70, p. 102628, 2025.

[125] G. Liu, T. Mao, Y. Tang, J. Zhao, and Z. Xiao, “Multiple-Mode Affine Frequency Division Multiplexing with Index Modulation,” 2025.

[126] H. S. Rou and G. T. F. de Abreu, “Chirp-permuted AFDM: A versatile waveform design for ISAC in 6G,” 2025.

[127] Y. I. Tek and E. Basar, “A Novel and Secure AFDM System for High Mobility Environments,” *IEEE Trans. Veh. Technol.*, pp. 1–6, 2025.

[128] H. Chen *et al.*, “Chirp Parameters Hopping over Time for Affine Frequency Division Multiplexing with Physical Layer Security,” in *Proc. IEEE ICC*, 2025, pp. 2120–2125.

[129] D. Zhang *et al.*, “Parameter Design for Secure Affine Frequency Division Multiplexing Waveform,” 2025.

[130] V. Savaux *et al.*, “On the Noise Robustness of Affine Frequency Division Multiplexing: Analysis and Applications,” in *Proc. of 6GNet*, December 2025, pp. 1–8.

[131] V. M. Reddy and H. Bitra, “PAPR in AFDM: Upper Bound and Reduction With Normalized μ -Law Companding,” *IEEE Access*, vol. 13, pp. 86 553–86 561, 2025.

[132] A. Ali, A. Arous, and H. Arslan, “Spreading the Wave: Low-Complexity PAPR Reduction for AFDM and OCDM in 6G Networks,” *IEEE Transactions on Green Communications and Networking*, vol. 10, pp. 1565–1577, 2026.

[133] H. Yuan *et al.*, “PAPR Reduction With Pre-Chirp Selection for Affine Frequency Division Multiplexing,” *IEEE Wireless Commun. Lett.*, vol. 14, no. 3, pp. 736–740, March 2025.

[134] Z. Lu, M. El-Hajjar, and L. liang Yang, “Augmented Affine Frequency Division Multiplexing for Both Low PAPR Signaling and Diversity Gain Protection,” 2025.

[135] M. Karthiga and D. Deepa, “PAPR reduction scheme in AFDM by optimal chirp selection using unimodular quadratic program,” *Physical Communication*, vol. 72, pp. 102731, 2025.